J. Fluid Mech. (2017), *vol.* 828, *pp.* 196–235.
doi:10.1017/jfm.2017.504

Effect of an internal nonlinear rotational dissipative element on vortex shedding and vortex-induced vibration of a sprung circular cylinder

Ravi Kumar R. Tumkur[1,†], Arne J. Pearlstein[2], Arif Masud[3], Oleg V. Gendelman[4], Antoine B. Blanchard[1], Lawrence A. Bergman[1] and Alexander F. Vakakis[2]

[1]Department of Aerospace Engineering, University of Illinois at Urbana-Champaign, IL 61801, USA

[2]Department of Mechanical Science and Engineering, University of Illinois at Urbana-Champaign, IL 61801, USA

[3]Department of Civil and Environmental Engineering, University of Illinois at Urbana-Champaign, IL 61801, USA

[4]Faculty of Mechanical Engineering, Technion-Israel Institute of Technology, Haifa 3200003, Israel

(Received 19 May 2016; revised 5 July 2017; accepted 19 July 2017;
first published online 31 August 2017)

We computationally investigate coupling of a nonlinear rotational dissipative element to a sprung circular cylinder allowed to undergo transverse vortex-induced vibration (VIV) in an incompressible flow. The dissipative element is a 'nonlinear energy sink' (NES), consisting of a mass rotating at fixed radius about the cylinder axis and a linear viscous damper that dissipates energy from the motion of the rotating mass. We consider the Reynolds number range $20 \leqslant Re \leqslant 120$, with Re based on cylinder diameter and free-stream velocity, and the cylinder restricted to rectilinear motion transverse to the mean flow. Interaction of this NES with the flow is mediated by the cylinder, whose rectilinear motion is mechanically linked to rotational motion of the NES mass through nonlinear inertial coupling. The rotational NES provides significant 'passive' suppression of VIV. Beyond suppression however, the rotational NES gives rise to a range of qualitatively new behaviours not found in transverse VIV of a sprung cylinder without an NES, or one with a 'rectilinear NES', considered previously. Specifically, the NES can either stabilize or destabilize the steady, symmetric, motionless-cylinder solution and can induce conditions under which suppression of VIV (and concomitant reduction in lift and drag) is accompanied by a greatly elongated region of attached vorticity in the wake, as well as conditions in which the cylinder motion and flow are temporally chaotic at relatively low Re.

Key words: chaos, vortex shedding, flow–structure interactions

† Email address for correspondence: tumkur.ravikumar@gmail.com

1. Introduction

Vortex-induced vibration (VIV) of a rigid cylinder is of practical importance in a range of applications involving flow past bluff bodies (Bearman 1984). Considerable effort has been devoted to active and passive VIV suppression, and to understanding the fundamental flow physics of how the motion of a linearly sprung cylinder is coupled to the dynamics of the wake, including the alternate shedding of vortices that gives rise to, and is modified by, the VIV. In addition to VIV suppression, there is also active interest in harnessing VIV in marine, riverine and estuarine flows to generate electrical power (Lee & Bernitsas 2011). Beyond these applications, VIV of a circular cylinder has come to be the prototypical system for studying bluff-body VIV. The case of greatest interest has been transverse VIV of a circular cylinder in rectilinear motion perpendicular to the mean flow. Recent reviews have been provided by Sarpkaya (2004), Williamson & Govardhan (2004), Gabbai & Benaroya (2005), Bearman (2011) and Païdoussis, Price & de Langre (2011).

We have recently investigated (Tumkur *et al.* 2013) how transverse VIV of a circular cylinder at and near $Re = UD/\nu = 100$ (where U, D and ν are the free-stream velocity, cylinder diameter and kinematic viscosity, respectively) restrained by a linear spring can be suppressed by attachment of a 'nonlinear energy sink' (NES) consisting of an essentially nonlinear spring (for which the force–displacement relation has no term linear in displacement, and hence has no linearized natural frequency) connecting the cylinder to a small mass from whose rectilinear motion, parallel to the transverse motion of the cylinder, energy is extracted and dissipated by a linear viscous damper. More generally, an NES is a dissipative attachment with strong (in fact, non-linearizable) stiffness and/or inertial nonlinearity, which, as discussed below, can passively absorb vibrational energy from the primary structure to which it is attached over broad frequency and energy ranges. The resulting nonlinear energy transfer from the structure to the NES has been dubbed 'targeted energy transfer' (TET), and consists of a nearly one-way (irreversible) transfer of energy from the primary vibrating structure (in this case the cylinder) to the mass of the NES (Vakakis *et al.* 2008), from which energy is dissipated, without 'spreading back' to the primary system. The nonlinear mechanism responsible for TET is isolated, or cascades of, transient resonance capture (Arnol'd 1988) realized over broad frequency and energy ranges. As shown by Tumkur *et al.* (2013), TET to the rectilinear NES can effect significant suppression of transverse VIV of a circular cylinder for small values of the ratio of the NES mass per unit length to the cylinder mass per unit length.

Besides the 'rectilinear NES' considered by Tumkur *et al.* (2013), there are many ways to passively affect VIV of a sprung cylinder by attaching 'lumped' masses and dampers. Here, we investigate an approach considered in a finite-dimensional, purely structural system by Gendelman *et al.* (2012), who showed that vibration of a primary structure can be effectively suppressed using TET to a small mass, from whose rotation at a fixed radius about an axis fixed in the primary structure, energy is dissipated by a linear damper. The essential nonlinearity is due to inertial coupling of rotation of the NES mass to rectilinear motion of the primary structure. As with the rectilinear NES (Tumkur *et al.* 2013), a rotational NES can be placed within a hollow cylinder or at one or both of a cylinder's ends, allowing VIV modification with no internal 'plumbing' (as required for approaches employing blowing and suction), and without external geometric changes (i.e. shrouds, helical appendages, freely rotatable plates or fairings) to the wetted surface. This, and the inherent attractiveness of a passive approach (i.e. no need for a feedback control system, electronics or a power supply), combine to make this a potentially attractive approach to VIV modification.

The work of Tumkur *et al.* (2013) for a rectilinear NES, which also included results for a 'tuned mass' linear proportional damper, dealt largely with suppressing VIV. Here, for a rotational NES, we focus on how such an element gives rise to several qualitatively different results for the flow, beyond VIV suppression. Specifically, a rotational NES can lead to temporal chaos in both the cylinder motion and flow at Reynolds numbers where flow past a fixed circular cylinder or NES-less sprung cylinder is time periodic. A rotational NES can also give rise to considerable elongation of the region of attached vorticity during each shedding cycle. Chaotic response in the wake of an oscillating cylinder at relatively low Re has potential application to enhancement of mixing and chemical reaction rates (see Deshmukh & Vlachos 2005), and has been considered in the context of flow past a periodically excited cylinder at higher Re by Karniadakis & Triantafyllou (1989), Batcho & Karniadakis (1991) and Leontini, Thompson & Hourigan (2006). The capability of this approach to enhance mixing and reaction rates in laminar flow, without forced excitation, is potentially attractive. A second result is that a rotational NES can induce VIV under conditions where an NES-less sprung cylinder does not undergo VIV.

While flow and the associated VIV in the laminar two-dimensional regime are expected to differ from behaviour at higher Re, traditionally of interest in applications (Anagnostopoulos & Bearman 1992), the laminar flow phenomena that we investigate are of interest for two main reasons. First, at $Re = 100$, the flow can be simulated without concern for the unresolved scales and attendant unmodelled dynamics associated with simulations of turbulent flow. Second, as shown by Roshko (1954), one notable feature of flow past a fixed cylinder is that the Strouhal number $St = f_s D/U$ (a dimensionless shedding frequency, where f_s is a properly defined dimensional shedding frequency) maintains a nearly constant value ($St = 0.19 \pm 0.02$) over $10^2 \leqslant Re \leqslant 10^4$, i.e. from the laminar two-dimensional regime well into the turbulent regime. As discussed by Roshko and by Williamson (1996), significant aspects of vortex shedding by a cylinder are qualitatively similar over wide ranges of Re, including at least part of the laminar regime. Thus, there is reason to believe that an understanding of the flow, of VIV and of approaches to modifying VIV at $Re = 100$, will be useful or can be adapted for use at much higher Re.

The remainder of the paper is organized as follows. In § 2 we briefly describe the physical model, governing equations and numerical methods. A stability boundary is presented in § 3, followed by results for the dynamic response in § 4 and characterization of the temporal chaos in § 5. In § 6, we show how an approximate analysis of the system, and an 'NES-induced mass' concept can be used to explain some of the results, and briefly discuss experimental realization. Some conclusions are offered in § 7.

2. Physical model, governing equations and computational approach

2.1. *Physical model and governing equations*

The physical model is that of a Newtonian fluid with constant density ρ_f and kinematic viscosity ν flowing with uniform and steady free-stream velocity $U\boldsymbol{e}_x$ past a rigid circular cylindrical surface of diameter $D = 2R$ with generators parallel to the z-axis. Rectilinear motion of the cylinder in the y-direction is driven by unsteady lift due to vortex shedding asymmetric about any constant-y plane, and is restrained by a linear spring. Flow past a motionless circular cylinder is known to be two-dimensional for Re up to approximately 190 (Williamson & Roshko 1988), and we assume, as have others (cf. Baek & Sung 2000), that the flow past an oscillating cylinder is also

two-dimensional in the regime of interest. As the cylinder moves, so do its component masses: a non-rotating stator with mass $\hat{M}_{stat}$ per unit length; and a rotating part with mass $\hat{M}_{rnes}$ per unit length not symmetrically distributed about the translating cylinder axis, about which it rotates at a fixed distance. Inertial coupling transfers energy from the stator to the rotating mass, from whose motion it is extracted and dissipated by a linear damper. We refer to the rotating mass and its damper as a 'rotational NES'.

The flow is governed by the Navier–Stokes equations, written dimensionlessly in terms of primitive variables as

$$\frac{\partial \boldsymbol{v}^*}{\partial \tau} + \boldsymbol{v}^* \cdot \boldsymbol{\nabla}^* \boldsymbol{v}^* = -\boldsymbol{\nabla}^* p^* + \frac{1}{Re} \boldsymbol{\nabla}^{*2} \boldsymbol{v}^*, \tag{2.1a}$$

$$\boldsymbol{\nabla}^* \cdot \boldsymbol{v}^* = 0, \tag{2.1b}$$

subject to the boundary conditions

$$\boldsymbol{v}^*|_{cyl} = \frac{\mathrm{d}Y_1^*}{\mathrm{d}\tau} \boldsymbol{e}_y \tag{2.1c}$$

and

$$\lim_{r \to \infty} \boldsymbol{v}^* = \boldsymbol{e}_x, \tag{2.1d}$$

where the dimensionless time is defined by $\tau = tU/D$ and we have scaled length (including the cylinder displacement $y_1 = Y_1^* D$), velocity (including the cylinder velocity on the right-hand side of (2.1*c*)) and pressure by D, U and $\rho_f U^2/2$, respectively. Here, an asterisk denotes a dimensionless quantity.

A schematic of the rotational NES attached to the cylinder is shown in figure 1. The coordinates x and y are referred to the centre of the undisplaced cylinder. Following the model of Gendelman *et al.* (2012), we take the rotating mass to be concentrated at a point or along a line a distance r_o from the cylinder axis. (Experimental realization for a rotating distributed mass is discussed in § 6.3.) The dimensional equations of motion for the coupled cylinder–NES system shown in figure 1 are written as

$$(\hat{M}_{stat} + \hat{M}_{rnes}) \frac{\mathrm{d}^2 y_1}{\mathrm{d}t^2} + \hat{K}_{cyl} y_1 = \hat{F}_L + \hat{M}_{rnes} r_o \frac{\mathrm{d}}{\mathrm{d}t} \left(\frac{\mathrm{d}\theta}{\mathrm{d}t} \sin\theta \right), \tag{2.2a}$$

$$\hat{M}_{rnes} r_o^2 \frac{\mathrm{d}^2 \theta}{\mathrm{d}t^2} + \hat{C}_{rnes} \frac{\mathrm{d}\theta}{\mathrm{d}t} = \hat{M}_{rnes} r_o \frac{\mathrm{d}^2 y_1}{\mathrm{d}t^2} \sin\theta, \tag{2.2b}$$

where $y_1(t)$ is the cylinder displacement relative to its equilibrium position and $\theta(t)$ is the angular position of the NES mass, increasing clockwise, with $\theta = \pi/2$ being along the positive x-axis. Here, $\hat{M}_{stat}$, $\hat{M}_{rnes}$ and $\hat{K}_{cyl}$ are the mass of the stator, the mass of the rotating part of the NES and the stiffness of the linear spring, respectively, and $\hat{F}_L$ is the dimensional lift force

$$\hat{F}_L = \int_0^{2\pi} \left[\left(-p + 2\mu \frac{\partial v_r}{\partial r} \right) \sin\phi + \mu \left(\frac{\partial v_\phi}{\partial r} - \frac{v_\phi}{r} + \frac{1}{r} \frac{\partial v_r}{\partial \phi} \right) \cos\phi \right] \Bigg|_R R \, \mathrm{d}\phi \tag{2.3}$$

each per unit length of cylinder, v_r and v_ϕ are the radial and azimuthal components of the fluid velocity on the cylinder surface, respectively, and r and ϕ are the radial and azimuthal coordinates, respectively. The damping of the rotational motion of the NES

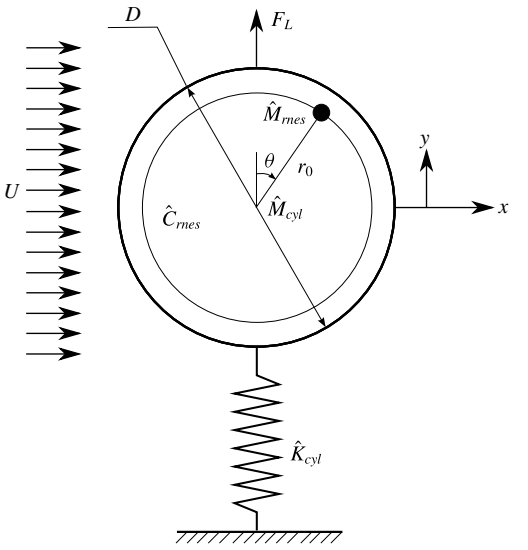

FIGURE 1. Cylinder in cross-flow with rotational NES. The rotational motion of the NES mass (at a fixed radius r_0, shown here for $r_0 < D/2$) is retarded by a linear viscous damper (not shown). The 'ground' to which the spring connects the cylinder should not be thought of as part of the boundary of the domain. The cylinder mass per unit length is defined by $\hat{M}_{cyl} = \hat{M}_{stat} + \hat{M}_{rnes}$.

mass attributable to the linear viscous damper, per unit length of cylinder, is denoted by $\hat{C}_{rnes}$. The absence of a gravitational force acting on the NES mass is tantamount to the cylinder axis being vertical.

Rotational motion of the NES mass is inertially coupled to transverse rectilinear motion of the cylinder through the second term on the right-hand side of (2.2*a*) and the right-hand side of (2.2*b*). For either of the two equilibrium solutions $(y_1(t), \theta(t)) = (0, 0)$ and $(0, \pi)$, this coupling is essentially nonlinear, in the sense that Taylor expansion of either inertial coupling term has no linear term. For these two equilibria, the dynamics of this system is strongly nonlinear and the rotational NES has no linear resonance. The absence of a linear term in these coupling terms, and dissipation (provided here by the linear viscous damper), is the prerequisites for TET (Vakakis *et al.* 2008) from the cylinder to the NES.

Defining $m^* = \rho_b/\rho_f$ and the three NES parameters $\epsilon_p = \hat{M}_{rnes}/(\hat{M}_{stat} + \hat{M}_{rnes})$ (a mass ratio), $\bar{r}_o = r_o/D$ and $\zeta_r = \hat{C}_{rnes}/(\nu \bar{r}_o^2 \hat{M}_{rnes})$ (a dimensionless damping coefficient), we non-dimensionalize (2.2*a*) and (2.2*b*) to get

$$\frac{\mathrm{d}^2 Y_1}{\mathrm{d}\tau^2} + (2\pi f_n^*)^2 Y_1 = \frac{2C_L}{\pi m^*} + \epsilon_p \bar{r}_o \frac{\mathrm{d}}{\mathrm{d}\tau}\left(\frac{\mathrm{d}\theta}{\mathrm{d}\tau}\sin\theta\right), \tag{2.4a}$$

$$\frac{\mathrm{d}^2\theta}{\mathrm{d}\tau^2} + \frac{\zeta_r}{Re}\frac{\mathrm{d}\theta}{\mathrm{d}\tau} = \frac{1}{\bar{r}_o}\frac{\mathrm{d}^2 Y_1}{\mathrm{d}\tau^2}\sin\theta, \tag{2.4b}$$

where $\rho_b = (\hat{M}_{stat} + \hat{M}_{rnes})/(\pi R^2)$ is the mean density of the cylinder, the lift force per unit length $\hat{F}_L$ in (2.2*a*) has been non-dimensionalized in favour of a lift coefficient C_L, and we have dropped the asterisk for the dimensionless cylinder displacement, now

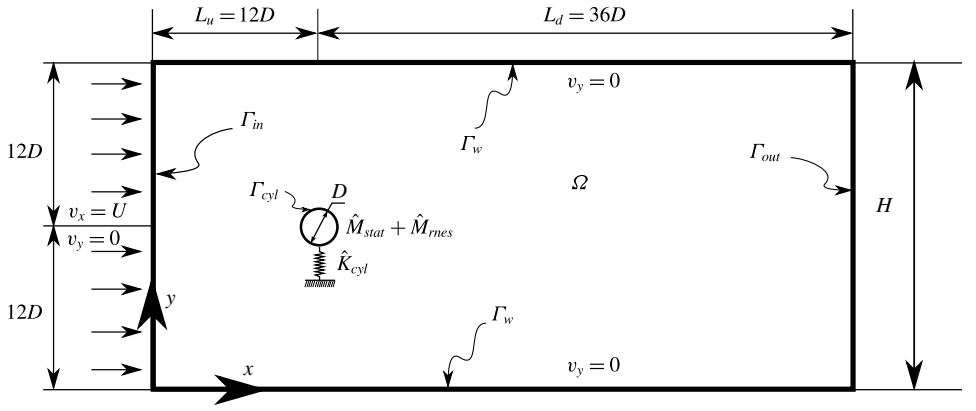

FIGURE 2. Computational domain.

denoted by Y_1. We have defined the dimensionless natural frequency of the sprung cylinder by

$$f_n^{*2} = \frac{1}{4\pi^2}\frac{D^2}{U^2}\frac{\hat{K}_{cyl}}{\hat{M}_{stat} + \hat{M}_{rnes}}. \tag{2.5}$$

We note that mechanical damping, parametrized by ζ_r, plays a rather different role here than in other analyses of VIV (Blackburn & Henderson 1996; Leontini *et al.* 2006). In those cases, rectilinear motion of the cylinder is directly damped by a term linearly proportional to $\mathrm{d}Y_1/\mathrm{d}t$ in an equation analogous to (2.4*a*) so that in the heavily damped limit, the cylinder motion is necessarily suppressed. For a cylinder with a rotating NES, however, damping acts on, and suppresses, the rotation of the NES mass. Thus, in the limit of large ζ_r in (2.4*a*), it is the rotation of the NES mass that is suppressed, with the dynamics of the cylinder approaching that of 'standard VIV' (i.e. a cylinder with no NES), in which case the NES extracts essentially no kinetic energy from the rectilinear motion of the cylinder. Thus, very large values of the damping parameter ζ_r correspond to essentially no NES-induced damping of the rectilinear motion of the cylinder.

In everything that follows, $m^* = 10$, a value chosen to facilitate validation of results by comparison to previous work. Except for one case discussed in § 4.1, the initial NES angular displacement and velocity are $\theta(0) = \pi/2$ and $\mathrm{d}\theta(0)/\mathrm{d}t = 0$, respectively. We take $f_n^* = 0.167$ unless otherwise specified. We note that for $m^* = 10$, the difference between f_n^* and an 'effective' natural frequency accounting for added mass effects is small.

2.2. *Computational approach*

Except as indicated below, the results shown were computed using the approach discussed in detail by Tumkur *et al.* (2013). Briefly, we employ a time-dependent annular domain (figure 2) whose cross-stream and streamwise extents are $24D$ and $48D$, respectively, and which deforms with cylinder motion. The centre of the cylinder moves on a line $36D$ upstream from the outlet. At the inlet and sidewall boundaries, the velocity is prescribed as its free-stream value. We prescribe a stress-free condition at the outlet, and a no-slip condition on the cylinder. The

Navier–Stokes equations are solved numerically in an arbitrary Lagrangian Eulerian (ALE) framework, discussed in detail by Calderer & Masud (2010) and references cited therein. The domain is discretized using a finite-element mesh, one element thick in the spanwise direction, with 8261 brick elements, corresponding to 16 922 nodes. The discretized Navier–Stokes equations are solved using the implicit second-order accurate generalized-α scheme discussed by Jansen, Whiting & Hulbert (2000) for first-order systems, in which the parameter ρ_∞ is set to 0. The rigid-body equations (2.4*a*) and (2.4*b*) and Navier–Stokes equations (2.1*a*) and (2.1*b*) are solved in a staggered fashion as described by Tumkur *et al.* (2013). The rigid-body equations are solved using the generalized-α scheme for second-order systems described by Chung & Hulbert (1993), with $\rho_\infty = 0$. To check whether the time step size was sufficiently small to achieve temporal convergence (especially with respect to the issue of fluid/structure interaction iteration), we needed to use a code that allows reduction of the time step size without increasing spatial resolution. To that end, all of the cases for which results are shown were recomputed using Nek5000 (Fischer, Lottes & Kerkemeier 2008), a spectral-element code which allows the time step size to be reduced without changing the spatial resolution (mesh and polynomial order). In several cases, finite-element results could not be reproduced using the spectral-element approach for the same values of $Re, m^*, f_n^*, \epsilon_p, \zeta_r$ and $\bar{r}_o$. In those cases, very similar results were obtained using the spectral-element approach for 'nearby' combinations of the parameters. For these cases (figures 6, 7, 14 and 16), the results presented were obtained for Nek5000. Spot checks showed that with the time step size ($\Delta\tau = 10^{-3}$) employed, no fluid–structure interaction iteration was necessary.

For cases in which the flow and rigid-body dynamics are chaotic, the details of solutions are extremely sensitive not only to initial conditions but also to computational parameters, such as spatial and temporal discretization, how iteration is conducted at each time step and on how the (parallel) computation is divided among processors. Detailed checks in selected cases show that the statistical properties (e.g. Fourier spectra, wavelet transformations, fractal dimension) of the solutions and the qualitative features (wake elongation, lift and drag reduction) we present are insensitive to those parameters and processes.

When there is no NES, the problem reduces to the well-known 'standard VIV case' of an elastically restrained cylinder in cross-flow. We have used this case, and the case of a fixed cylinder, to validate our finite-element code (Tumkur *et al.* 2013) and our spectral-element code (Tumkur *et al.* 2017). For a fixed cylinder at $Re = 100$, the spectral-element approach provides good convergence with respect to time step size, domain size, number of mesh elements and polynomial order, as shown in table S1, where the results of Henderson (1995) (including the unpublished results of Henderson, cited by Shiels, Leonard & Roshko (2001)) and Tumkur *et al.* (2013) are shown for comparison. For the linearly sprung cylinder at $Re = 100$ with $m^* = 10$ and $f_n^* = 0.167$, standard VIV with maximum dimensionless oscillation amplitude 0.49 was computed, in excellent agreement with the results of Prasanth & Mittal (2009) at the same Re, m^* and f_n^*.

3. Stability boundary

We first address the question of how the NES affects the stability of the steady solution, corresponding to symmetric flow past a motionless sprung cylinder whose stability has been considered recently by Tumkur *et al.* (2017) for $m^* = 10$. (We distinguish between the 'fixed-cylinder' case, in which the cylinder is not allowed to

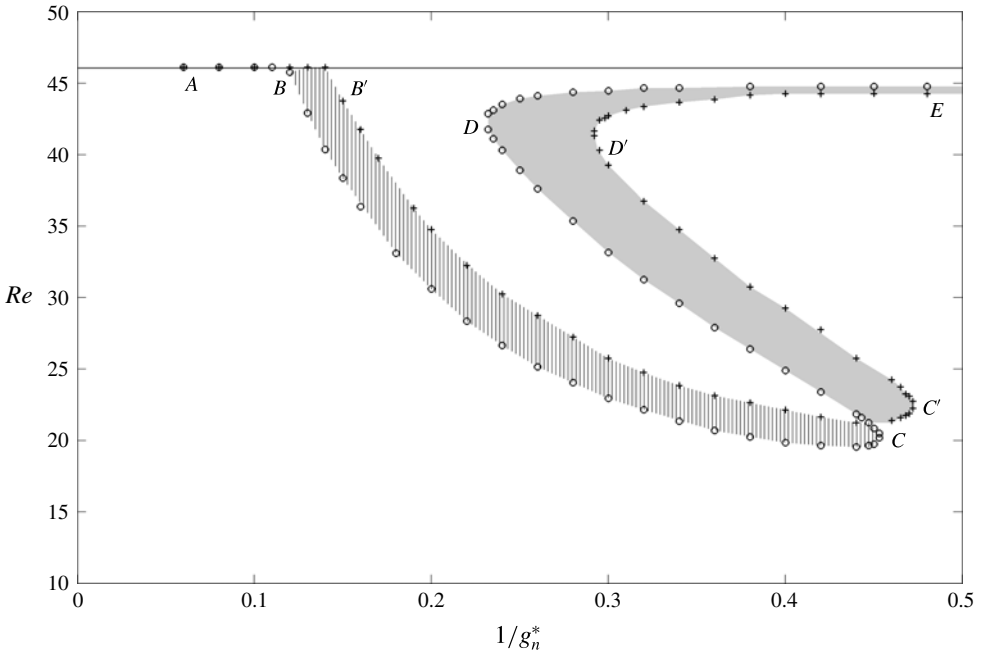

FIGURE 3. For $m^* = 10$, effect of an NES (with $\epsilon_r = 0.3$, $\zeta_r = 1.333$ and $\bar{r}_o = 0.3$) on the stability of the steady, symmetric motionless-cylinder solution with $\theta_s = \pi/2$. Points on the stability boundary are denoted by '○' for the NES-less sprung cylinder case (Tumkur *et al.* 2017), and by '+' with this NES for $\theta_s = \pi/2$. The line at $Re = 46.05$ is the critical value for a fixed cylinder, computed by Tumkur *et al.* (2017). In the vertically lined region and shaded region, this NES (with $\theta_s = \pi/2$) stabilizes and destabilizes, respectively, the steady, symmetric, motionless-cylinder solution with respect to the NES-less linearly sprung case.

move, and the 'motionless-cylinder' case, in which a sprung cylinder does not move, even though motion is allowed.) For the NES-less system, stability depends on the dimensionless natural frequency f_n^* of the spring/mass system, the density ratio m^* and Re. For a fixed value of m^*, the results can be represented in terms of critical values of Re as a function of some measure of the stiffness of the spring/mass system. We choose

$$g_n^* = f_n^* Re = (D^2/\nu)\sqrt{\hat{K}_{cyl}/(\hat{M}_{cyl} + \hat{M}_{rnes})}/(2\pi), \tag{3.1}$$

so that the dimensionless stiffness is independent of U, which is typically used to vary Re. (We note that the NES parameters ϵ_p, ζ_r and $\bar{r}_o$ are independent of U.) As discussed by Tumkur *et al.* (2017) and shown by the stability boundary *ABCDE* in figure 3 of the present work, the steady, symmetric, motionless-cylinder (SSMC) solution for flow past an NES-less sprung cylinder can be unstable well below the fixed-cylinder value of $Re_{crit,fixed} = 46.05$. In addition, as shown in figure 3, there is a range of g_n^* for which there are three critical values of Re ($Re_{lower} < Re_{middle} < Re_{upper}$), with the steady solution being stable for $Re < Re_{lower}$ and $Re_{middle} < Re < Re_{upper}$, and unstable for $Re_{lower} < Re < Re_{middle}$ and $Re > Re_{upper}$.

Tumkur *et al.* (2017) have rigorously proved, by considering the initial value problem for the sprung-cylinder case, that for each g_n^*, the SSMC solution is linearly

unstable for every Re for which steady flow past a fixed cylinder is unstable. Another key finding of Tumkur *et al.* (2017) is that the NES-less stability boundary (indicated by open circles) in figure 3 is single valued for sufficiently large and small values of $1/g_n^*$, and triple valued in an intermediate range of $1/g_n^*$. (For a circular cylinder with $m^* = 4.73$ undergoing VIV in the transverse and streamwise directions, with two independent restraining springs having the same spring constant, Mittal & Singh (2005) had previously identified two disjoint ranges of stable Re for a single value of the dimensionless spring constant.) Tumkur *et al.* (2017) also found that near the point where the NES-less stability boundary begins to descend as $1/g_n^*$ increases (near $Re = 46$, $1/g_n^* = 0.119$), the critical frequency associated with the Hopf bifurcation jumps discontinuously from a value corresponding to the Kármán vortex street (for $1/g_n^* < 0.119$) to a higher value associated with a 'structural' mode (for $1/g_n^* > 0.119$) corresponding to a double-Hopf point. Finally, just above the stability boundary, near the double-Hopf point, the response is quasi-periodic, with significant response at the frequencies associated with both the Kármán vortex street and structural modes.

The proof by Tumkur *et al.* (2017) that the SSMC solution of the (NES-less) sprung-cylinder problem is linearly unstable above the critical Re for a fixed cylinder can be directly extended to the NES-equipped case. To actually establish the stability boundary, however, requires considering the effects of the NES parameters (ϵ_p, ζ_r and $\bar{r}_o$), and also the fact that an SSMC solution exists for any NES displacement. However, as shown in Part B of the supplementary material available at https://doi.org/10.1017/jfm.2017.504, linearization of (2.1*a*), (2.1*b*), (2.4*a*) and (2.4*b*) about an SSMC solution with an NES displacement of θ_s leads to an eigenvalue problem in which ζ_r and $\epsilon_p \sin^2 \theta_s$ are the only dimensionless parameters beyond Re, m^* and f_n^*. In other words, while the solution of the initial value problem (and hence the dynamics) for the full nonlinear problem depends on Re, m^* and f_n^*, $\bar{r}_o$, ζ_r, ϵ_p and θ_s, linear stability of the SSMC solution depends only on Re, m^*, f_n^*, ζ_r and $\epsilon_p \sin^2 \theta_s$, and so the NES introduces only two additional independent parameters to the stability analysis, rather than four. In addition, equations (S14)–(S16) in the supplementary material show that if $\epsilon_p = 0$ or $\theta_s = n\pi$ (n an integer), then the NES has no effect on the linear stability analysis.

We consider the stability of the SSMC flow past an NES-equipped linearly sprung cylinder for one combination of NES parameters ($\epsilon_p = 0.3$, $\zeta_r = 1.333$ and $\bar{r}_o = 0.3$) for $\theta_s = \pi/2$. The stability boundary for the NES-equipped case pertains to an SSMC base flow, and was determined by adapting the approach described in Tumkur *et al.* (2017) for the NES-less case, along the lines described by Zielinska & Wesfreid (1995), in which eigenvalues are not computed. For the NES-less case, the base flow was judged to be stable if the long-time solution (computed using the full nonlinear equations) was an SSMC solution, for which sufficiently small asymmetric disturbances decayed for combinations of Re and $1/g_n^*$ on one side of the boundary $ABCDE$, and did not decay on the other side. The NES-equipped case requires inclusion of the NES angular position θ, and recognition that when an initial state with a non-zero θ is subjected to an infinitesimal disturbance, the long-time solution might be an SSMC solution with θ differing non-infinitesimally from the initial value. This can arise if the infinitesimal disturbance initially grows to 'finite amplitude', before settling as an SSMC with θ differing considerably from the initial value. For a hypothetical infinitesimal disturbance, we designate such a case as unstable, reserving 'stable' for the situation in which the final state is an SSMC with θ differing only infinitesimally from the initial value.

We consider only non-zero initial values of θ ($\theta = \pi/2$ unless otherwise indicated), and note that the stability boundary $AB'C'D'E$ separates situations where asymmetric

disturbances decay from those in which they do not. Any asymmetric disturbance will set the cylinder and NES into motion. (A symmetric inlet transient can also lead to instability, but only as a result of very small asymmetries in the numerics.) For the asymmetric non-infinitesimal disturbances we used, we expect a final value of θ differing only slightly from $\pi/2$ to arise only as a limiting case when the asymmetry of the inlet transient tends to zero. All of the results were computed with an inlet transient

$$v_x(0, y^*, \tau) = [1 + q\mathrm{e}^{-(y^*-1)^2/2}](1 - \tau/25) + \tau/25 \quad 0 \leqslant \tau \leqslant 25 \tag{3.2}$$

having very small asymmetry $\left(q = 10^{-4}\right)$. Spot checks on the stable side of the stability boundary gave final values of θ that exceeded $\pi/2$ by very small amounts. For example, at $Re = 25$ and $1/g_n^* = 0.3$, 'asymmetry amplitudes' of $q = 10^{-1}$, 10^{-2}, 10^{-3} and 10^{-4} gave final value of θ that exceeded $\pi/2$ by 8.48×10^{-5}, 5.20×10^{-8}, 1.61×10^{-9} and 0, respectively. (The value for $q = 10^{-4}$ is limited by the number of significant figures used to report the final θ.) This shows that base states characterized as stable are SSMC solutions for which the final value of θ approaches $\pi/2$ as the asymmetry of the inlet transient approaches zero. This, in turn, provides a high degree of confidence that the stability boundary shown is indeed the linear stability boundary.

Figure 3 shows that for the given NES parameters, the stability boundary $AB'C'D'E$ (points on which are denoted by the symbol '+') is qualitatively similar to that for the NES-less sprung cylinder. As in that case, the stability boundary is single valued for $1/g_n^* < 1/g_{n,D'}^*$ and for $1/g_n^* > 1/g_{n,C'}^*$, and triple valued in the intermediate range $1/g_{n,D'}^* < 1/g_n^* < 1/g_{n,C'}$ where C' and D' are the counterparts of the left and right turning points found in the NES-less case (Tumkur *et al.* 2017).

For $\theta_s = \pi/2$, figure 3 also shows that the region in the $1/g_n^* - Re$ plane in which the NES-equipped sprung cylinder is linearly stable is not a subset of the region in which the NES-less sprung cylinder is stable. In regions where the NES-less case is unstable and flow past the NES-equipped sprung cylinder is linearly stable (vertically lined region in figure 3), rectilinear cylinder motion will cause the NES mass in any initial position other than an integer multiple of π to rotate, which will cause the NES to dissipate energy through the damper, with the potential for the system to asymptotically approach the SSMC solution. On the other hand, in regions where the NES-less case is linearly stable and flow past the NES-equipped sprung cylinder with $\theta_s = \pi/2$ is unstable (shaded area in figure 3), the NES destabilizes the flow. In that case, transfer of kinetic energy between the rotation of the NES mass and the rectilinear motion of the cylinder allows for disturbance growth (and sustainment of motion) that cannot be overcome by dissipation through the damper of the NES. In summary, we see that introduction of an NES can either destabilize the SSMC solution, or completely suppress VIV.

The NES has the effect of shifting the double-Hopf point (denoted by B for the NES-less sprung-cylinder case, and by B' for the NES parameters specified above) to a larger value of $1/g_n^*$, which we estimate to be 0.140, based on extrapolation of results at $1/g_n^* = 0.15$, 0.16, 0.17, 0.19 and 0.20. Compared to the NES-less sprung-cylinder case, the right turning point C' is at slightly larger values of $1/g_n^*$ and Re, while the left turning point D' is displaced to a larger value of $1/g_n^*$, with a small change in Re. The asymptotic behaviour as $1/g_n^* \to 0$ and as $1/g_n^* \to \infty$ seems to be virtually unchanged compared the NES-less case.

For most combinations of $1/g_n^*$ and Re for which the SSMC solution with $\theta_s = \pi/2$ is unstable for this NES-equipped case, the long-time attracting two-dimensional

solution is time periodic. We have found two exceptions. First, quasi-periodic and temporally chaotic solutions are found in several ranges of $1/g_n^*$ and Re, as in the NES-less spring-cylinder case. Second, in a portion of the triple-valued range of $1/g_n^*$, the lower interval of unstable Re ($Re_{lower} < Re < Re_{middle}$) includes a subinterval of Re in which disturbance growth is oscillatory with an exponential envelope, but the disturbance then decays to zero (without approaching a 'stationary' oscillatory state) in an oscillatory fashion with an exponentially decaying envelope, approaching an SSMC solution in which $\theta_s = n\pi$ (i.e. the final orientation of the NES mass is displaced 90° from its initial position).

As mentioned above, if θ_s is an integer multiple of π, then the NES has no effect on the linear stability analysis and the stability boundary will be identical to that for the NES-less case. On the other hand, as θ_s varies, we expect a continuous deformation of the NES-less stability boundary (points denoted by '○' in figure 3 for $\theta_s = 0$) into the $\theta_s = \pi/2$ curve (points denoted by '+').

Finally, the issue arises as to how the critical values of Re might be determined experimentally. There are two key questions. First, will three-dimensional effects render the two-dimensional analysis moot? Second, what is the importance of nonlinearity, and in particular, subcritical onset?

Three-dimensionality can become an issue in two ways. First, even a slightly three-dimensional geometry (e.g. any finite-span cylinder) can give rise to oblique shedding (Williamson 1989). This will probably require use of a large aspect ratio cylinder. Second, there is the potential for three-dimensional instability in a strictly two-dimensional base flow (Williamson & Roshko 1988; Leontini, Thompson & Hourigan 2007). Fortunately, work by Leontini *et al.* (2007) strongly suggests that two-dimensional flow past a circular cylinder undergoing either transverse VIV or forced transverse oscillation becomes unstable with respect to three-dimensional disturbance at Re above the known fixed-cylinder critical value of 190 (Williamson & Roshko 1988). To assess the significance of these three-dimensional effects in detail would require a three-dimensional analysis, which is beyond the scope of the present work.

At its heart, the question of nonlinearity in the stability analysis is one of whether there are accessible combinations of initial conditions and inlet conditions for which the trajectory is attracted to solutions consistent with the (linear) stability boundary. The extensive computations mentioned above do indeed confirm that there are simple asymmetric inlet transients and initial conditions that lead to an SSMC solutions in the stable portion of figure 3, and to unsteady VIV solutions in the unstable portion, with the boundaries between the two corresponding to the critical Re values shown in figure 3. These results suggest that nonlinearity will not be a serious impediment to experimental verification of the critical values.

4. Dynamic response

Here, we explore how addition of a mass whose damped rotational motion about the cylinder axis is inertially coupled to the rectilinear motion of the cylinder can significantly affect cylinder motion and flow. The intent is to show the diversity of effects, rather than to focus on any of them (e.g. VIV suppression) or systematically survey the parameter space. To that end, results are described for only a few of the (ϵ_p, ζ_r, $\bar{r}_o$) combinations in an ensemble of several hundred computations. Unless otherwise specified, $Re = 100$.

Post-processing of some computed time series was performed by numerical wavelet transforms (WT) using an algorithm described by Grossmann & Morlet (1984) and

Argoul & Le (2003), employing only the Morlet wavelet, a Gaussian-windowed complex sinusoid. Choosing the frequency of the mother wavelet allows one to tune the temporal and frequency resolution of the results. In the WT contour plots (WT spectra) presented, we show the amplitude of the WT as a function of frequency (vertical axis) and time (horizontal axis). Heavily and lightly shaded areas correspond to regions of high and low WT amplitude, respectively. Such plots reveal temporal evolution of the frequency components of the time series, and allow identification of modal transitions as the system evolves (Vakakis *et al.* 2008). The WT contour plots can thus be regarded as 'dynamic analogues' of the classic Fourier transform, whose applicability is restricted to stationary signals and which provides the frequency content of a signal in an averaged sense.

4.1. *NES reduction of cylinder motion*

In this section, we show how interaction of NES rotation with the flow, mediated by the cylinder, leads to TET directed to the NES, resulting in suppression of cylinder vibration. Two passive suppression mechanisms were observed: a 'strongly modulated response' (SMR; 'Mechanism I') and a 'suppressed limit-cycle oscillation' (LCO; 'Mechanism II'). We made no effort to search for the best combination of, or to otherwise optimize, the NES parameters. The best passive suppression found in the original ensemble for each mechanism is reported in this section.

Strongly modulated responses – Mechanism I

For NES parameters $\bar{r}_o = 0.2$, $\epsilon_p = 0.3$ and $\zeta_r = 21.221$, the cylinder exhibits a strongly modulated response. The time history of the cylinder displacement, NES angle, NES angular velocity and lift coefficient are shown in figure 4(*a–d*). (In the results shown, the angular displacement of the NES mass is given in radians.) The root-mean-square (r.m.s.) cylinder displacement is reduced by approximately 71 % compared to the NES-less system. Figure 4(*b*,*c*) shows that as the cylinder undergoes relaxation oscillations, the direction of rotation of the NES mass changes, with a dominant frequency comparable to the modulation frequency of the cylinder displacement and lift coefficient. By comparison to figure 4, figure S1 in the supplementary material shows that for the stated combination of NES parameters, choosing $\theta(0) = \pi/4$ rather than $\theta(0) = \pi/2$ has the effect of temporally delaying development of instability, but has no qualitative effect on the long-time solution. Note, however, that as discussed in § 3, the stability of the SSMC solution depends on $\zeta \sin^2 \theta_s$, so that the strong similarity of the long-time solutions (evident by comparing the r.m.s. values of lift and cylinder displacement shown in figures 4 and S1) is not universal for all combinations of NES parameters.

Figure 5(*a–c*) shows the frequency content (in terms of WT spectra) of the time series of cylinder displacement, cosine of the NES angular displacement and lift coefficient shown in figure 4. The cylinder displacement and lift coefficient have a dominant frequency close to the natural shedding frequency, whereas the NES angular displacement has no dominant frequency, showing that the NES is not in a 1:1 resonance with the cylinder displacement or lift coefficient. Unlike the standard VIV case near $Re = 100$ (Prasanth & Mittal 2009), for which the WT is a strong horizontal band at the Strouhal frequency and a weaker band at its third harmonic, figure 5(*a–c*) shows that the response with a rotational NES is broadband. This is due to the NES's nonlinearizable inertial nonlinearity, which has no preferred resonance frequency and enables transient resonant capture over a broad range of frequency in the cylinder response.

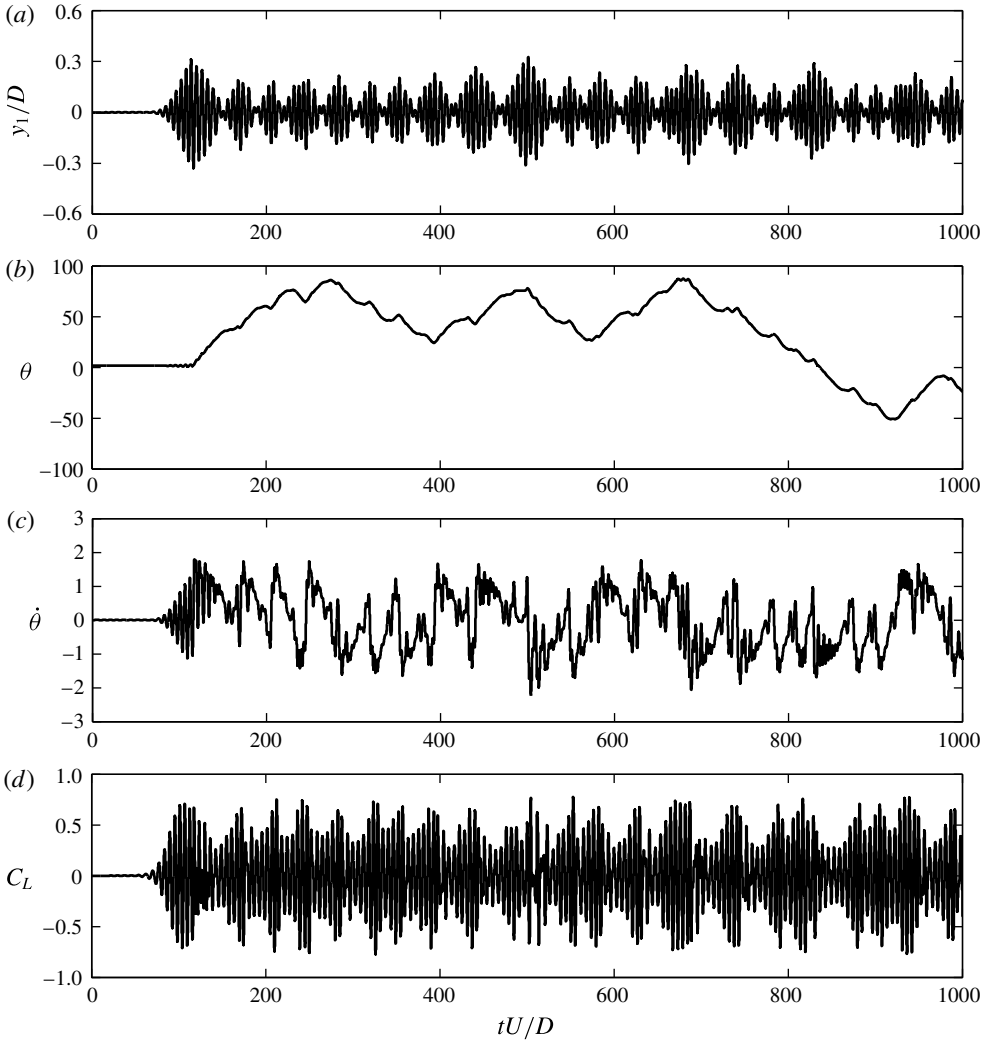

FIGURE 4. Mechanism I response with 71 % reduction in r.m.s. cylinder displacement for $Re = 100$, $\bar{r}_o = 0.2$, $\epsilon_p = 0.3$ and $\zeta_r = 21.221$. (*a*) Cylinder displacement (Y_1); (*b*) NES angle (θ); (*c*) NES angular velocity ($\dot{\theta}$); and (*d*) lift coefficient (C_L). Root-mean-square values of Y_1 and C_L for $200 \leqslant tU/D \leqslant 1000$ are 0.1245 and 0.3474, respectively.

The strongly modulated response is characterized by very deep modulation. In fact, the response amplitude oscillates between a maximum value and a minimum value close to zero. The strongly modulated response is ubiquitous in NES-equipped systems under external forcing or self-excitation, and is usually related to relaxation oscillations of the averaged slow flow on a slow invariant manifold (Gendelman 2011).

Suppressed LCO – Mechanism II

A different mechanism of passive VIV suppression is found for NES parameters $\bar{r}_o = 0.2$, $\epsilon_p = 0.3$ and $\zeta_r = 98.40$. The cylinder displacement, NES angle and lift coefficient are shown in figure 6(*a–c*), indicating that a reduction of approximately

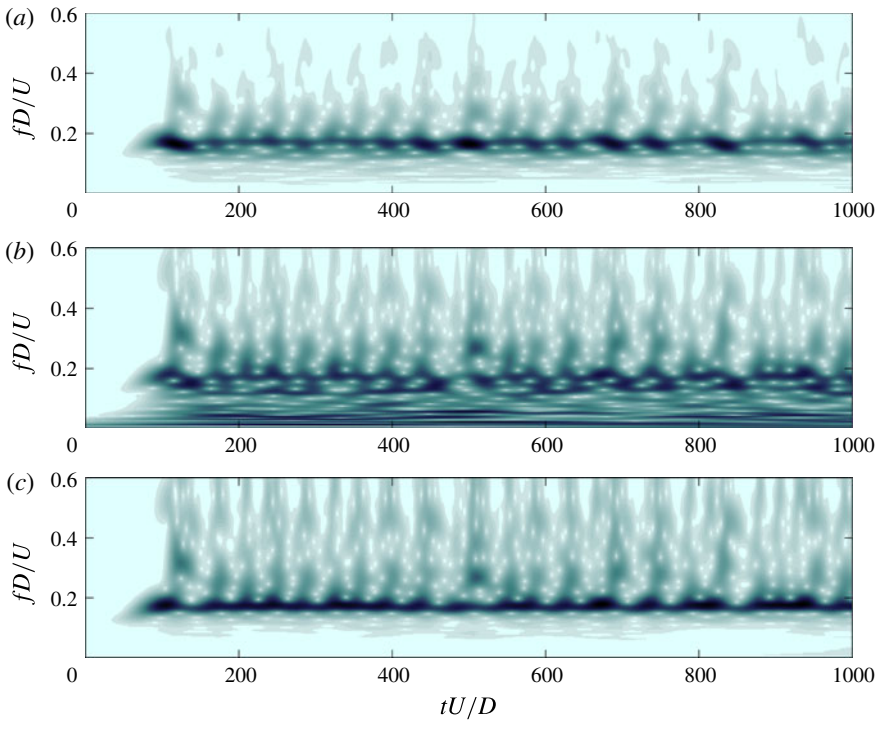

FIGURE 5. (Colour online) Frequency content of Mechanism I response with 71 % reduction in r.m.s. cylinder displacement for $Re = 100$, $\bar{r}_o = 0.2$, $\epsilon_p = 0.3$, and $\zeta_r = 21.221$. Wavelet transforms of (*a*) cylinder displacement (Y_1); (*b*) NES angle ($\cos\theta$); and (*c*) lift coefficient (C_L).

50 % in the r.m.s. cylinder displacement (to a maximum amplitude of approximately $0.25D$) can in this case be attributed to the rotational NES.

Figure 6(*b*) shows that the NES mass remains nearly motionless when the cylinder displacement is very small. Once the cylinder displacement reaches a sufficiently large amplitude, the NES starts interacting with the cylinder, and after an initial transient, the system settles into a 1:1:1 resonance, as seen from frequency analysis of the time series, shown in figure 7(*a–c*). We note that for Mechanism II, the direction of NES rotation reverses with a frequency one half that of the cylinder displacement and lift coefficient.

4.2. *Intermittent bursting and wake modification*

For $\bar{r}_o = 0.5$, $\epsilon_p = 0.3$ and $\zeta_r = 0.340$, the response is characterized by very slow decay of the cylinder displacement, angular velocity of the NES mass, oscillation amplitude of the drag coefficient and lift coefficient, followed by bursting into a chaotic mode, as shown in figure 8(*a–e*). Time integration in this 'slowly decaying chaotic burst' case was performed for a very long duration (4000 dimensionless convective time units) to ascertain the long-time nature of the solution. Figure 8(*a*) shows that cylinder displacement decays considerably (by approximately 80 %), the lift coefficient decreases by approximately 98 % and the oscillation amplitude of the drag coefficient decreases by nearly 100 %, before bursting into chaotic oscillation.

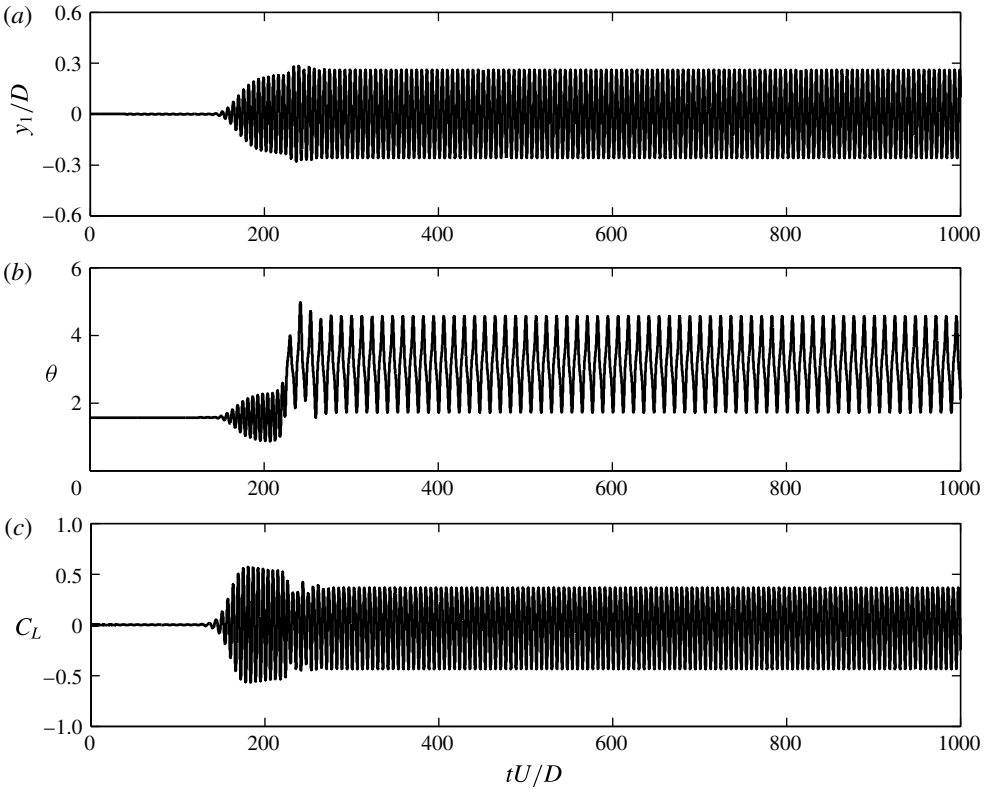

FIGURE 6. Mechanism II response with 50 % reduction in r.m.s. cylinder displacement for $Re = 100$, $\bar{r}_o = 0.2$, $\epsilon_p = 0.3$ and $\zeta_r = 98.40$. (*a*) Cylinder displacement (Y_1); (*b*) NES angle (θ); and (*c*) lift coefficient (C_L).

This slow decay followed by bursting into chaos recurs, strongly suggesting that the observed response in what we refer to as the 'intermittently bursting' solution is not an initial transient, but rather a stable attractor for this combination of NES parameters. Figure 8(*b*,*c*) shows that although a moving average of the angular displacement of the NES mass is nearly a piecewise linear function of time, the angular velocity of the NES mass has a low-amplitude, relatively high-frequency component. Figure 8(*c*) shows that rotation of the NES mass is nearly unidirectional during each interval of slow decay of the cylinder amplitude, with the direction resetting after each chaotic burst. This long-duration, nearly unidirectional rotation of the NES mass differs from that found for Mechanisms I and II, described in § 4.1.

The frequency content for the intermittently bursting solution is shown in figure 9. Unlike the SMR and LCO regimes discussed above, the frequency content deviates from the Strouhal frequency on a slow time scale. During the chaotic bursts, there is no dominant frequency, indicating that the response is essentially broadband. But once the system locks on to the slowly decaying response, there is clearly a dominant frequency close to the Strouhal frequency, for both the cylinder displacement (figure 9*a*) and NES angle (figure 9*b*), but not for the drag and lift coefficients (figure 9*c*,*d*).

A distinctive feature of this intermittently bursting solution is that the dominant frequency is no longer constant in time, but continuously decreases within the slowly

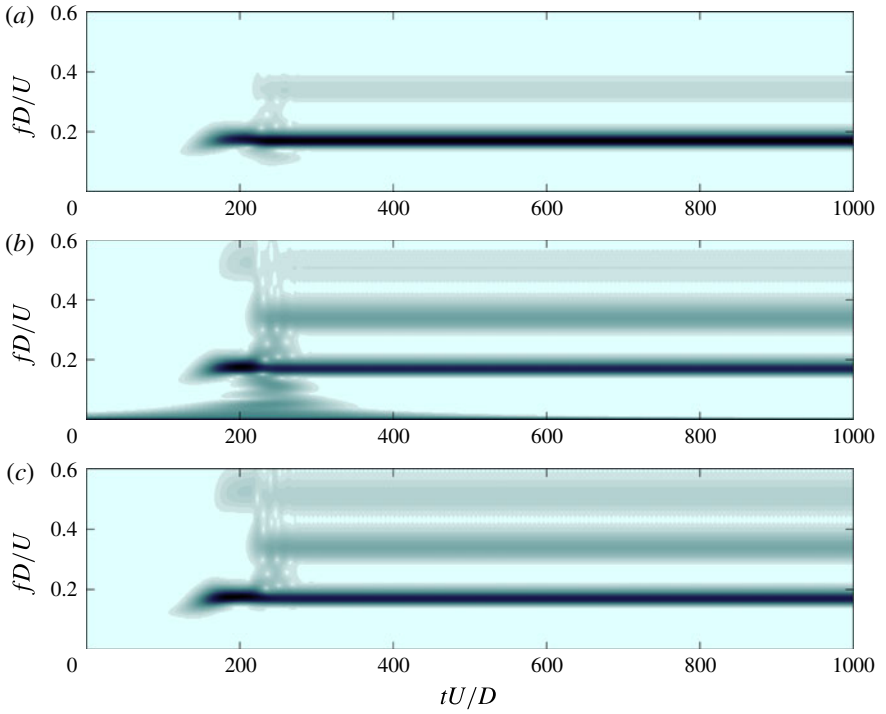

FIGURE 7. (Colour online) Frequency content of Mechanism II response with 50 % reduction in r.m.s. cylinder displacement for $Re = 100$, $\bar{r}_o = 0.2$, $\epsilon_p = 0.3$ and $\zeta_r = 98.40$. Wavelet transforms of (*a*) cylinder displacement (Y_1); (*b*) NES angle ($\cos\theta$); and (*c*) lift coefficient (C_L).

varying portion of the response, falling below *St* before each burst into chaos. The detuning from the Strouhal frequency is approximately 15 % at the beginning of the slow decay and reaches 33 % near the end. During the slow decay, the dominant frequency in C_L is approximately twice the Strouhal frequency. For NES-less VIV at higher *Re*, such a transition in lift frequency content has been attributed to switching in the timing of vortex shedding (Williamson & Roshko 1988), thus suggesting closer examination of the wake structure.

For $\bar{r}_o = 0.5$, $\epsilon_p = 0.3$ and $\zeta_r = 0.340$, figure 10(*a*) shows that at a time close to the end of the slow decay, there are striking changes in wake structure, not seen for other combinations of the NES parameters discussed in § 4.1, or for a rectilinear NES (Tumkur *et al.* 2013). It is well known that in two-dimensional standard VIV, the wake structure remains qualitatively similar to that of the fixed-cylinder case, with a well-defined Kármán vortex street. Indeed, in our computations for many other combinations of rotational NES parameters, and for a rectilinear NES (Tumkur *et al.* 2013), the vortex streets found are qualitatively very similar to those for standard VIV. However, for $\bar{r}_o = 0.5$, $\epsilon_p = 0.3$ and $\zeta_r = 0.340$, and for other values of the rotational NES parameters, the intermittently bursting solution is associated with elongation of the attached vorticity to about $10D$ aft of the rear of the cylinder, compared to approximately $4D$ and $4.5D$ for the stationary and standard VIV cases, respectively. (In all figures showing wake structure, the cross-stream and streamwise extents of the image are $5D$ and $36D$, respectively.)

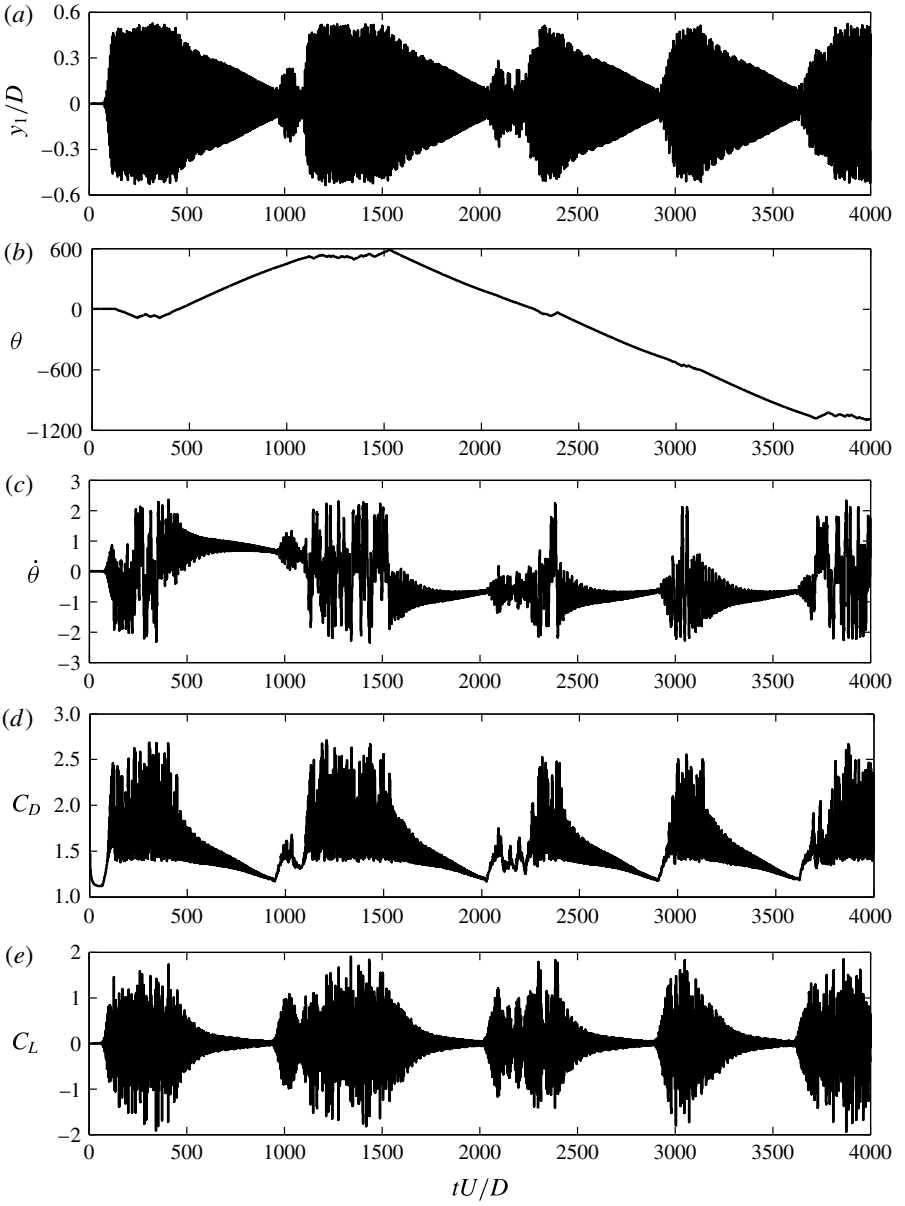

FIGURE 8. For $Re = 100$, $\bar{r}_o = 0.5$, $\epsilon_p = 0.3$ and $\zeta_r = 0.340$, time history of the slowly decaying and intermittently chaotic bursting response. (*a*) Cylinder displacement (Y_1); (*b*) NES angle (θ); (*c*) NES angular velocity ($\dot{\theta}$); (*d*) drag coefficient (C_D); and (*e*) lift coefficient (C_L).

Elongation of the region of attached vorticity is seen only when the cylinder oscillation amplitude envelope is slowly decaying. The wake structure is shown in figure 10(*a*) at $tU/D = 910.125$, just before bursting into the chaotic regime, and in figure 10(*b*) at $tU/D = 1181.375$, well into the chaotic regime. By comparing these results to those at $Re = 100$ for flow past a stationary cylinder shown in figure 10(*c*),

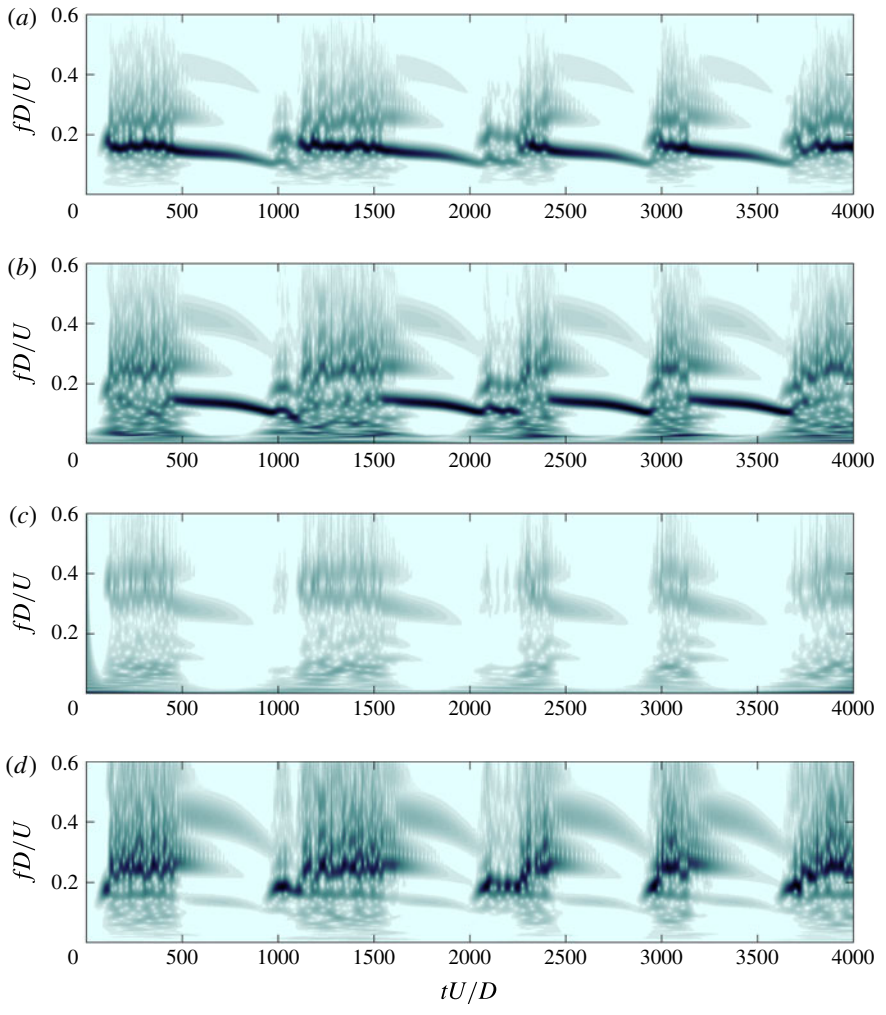

FIGURE 9. (Colour online) For $Re = 100$, $\bar{r}_o = 0.5$, $\epsilon_p = 0.3$ and $\zeta_r = 0.340$, frequency content of the slowly decaying and intermittently chaotic bursting response. Wavelet transforms of (*a*) cylinder displacement (Y_1); (*b*) NES angle ($\cos\theta$); (*c*) drag coefficient (C_D); and (*d*) lift coefficient (C_L).

and for standard (NES-less) VIV shown in figure 10(*d*), we see significant differences in the near and far wake. Compared to those cases, the region of attached vorticity in figure 10(*a*) is not only elongated, but also noticeably 'straightened', and the strength of the alternating vortices farther downstream is considerably diminished. These results suggest, as discussed in § 6.1, that the steady symmetric solution is in some sense 'partially stabilized' by action of the NES during the slow decay, and that as the flow becomes increasingly unsteady near the end of the slow decay, this partial stabilization is overcome, with the flow 'locking out' of the slowly decaying envelope.

As discussed above in connection with figure 8(*e*), the amplitude of C_L decreases by approximately 98 % during each slow decay cycle. Figure 11(*a–c*) compares time histories of C_L for the cylinder with a rotational NES (figure 11*a*, with finer temporal

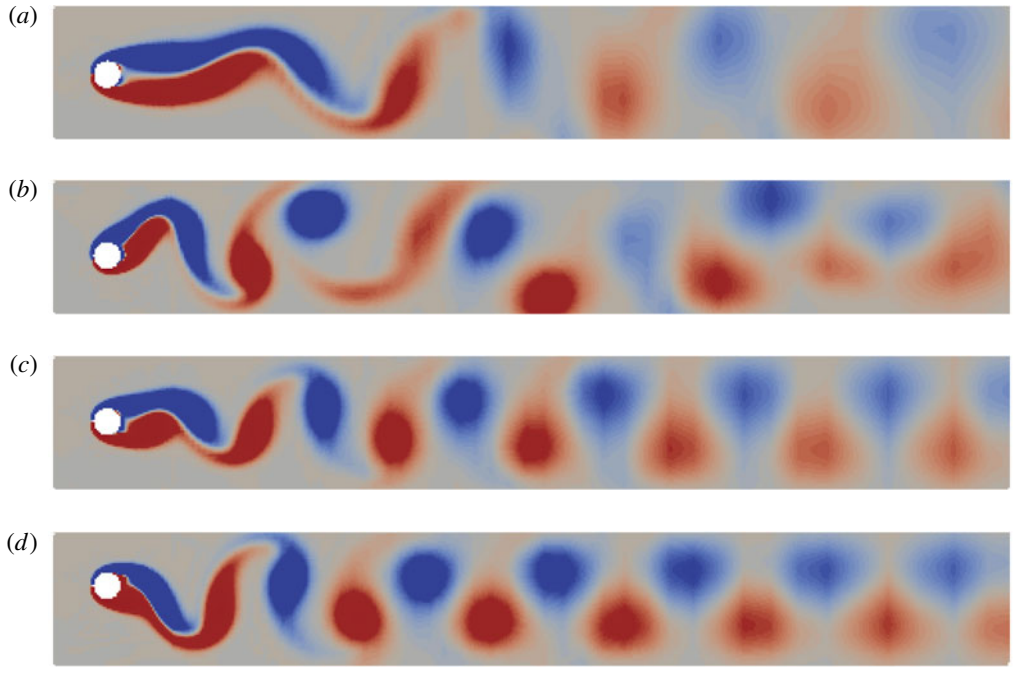

FIGURE 10. (Colour online) For $Re = 100$, spanwise vorticity (a) with NES ($\bar{r}_o = 0.5$, $\epsilon_p = 0.3$ and $\zeta_r = 0.340$) at $tU/D = 910.125$; (b) with NES ($\bar{r}_o = 0.5$, $\epsilon_p = 0.3$ and $\zeta_r = 0.340$) at $tU/D = 1181.375$; (c) for stationary cylinder; and (d) for free VIV without NES.

detail than shown in figure 8*e*), a stationary cylinder (figure 11*b*) and the NES-less VIV case (figure 11*c*). By comparison, the amplitude of the (periodic) C_L for the fixed cylinder (figure 11*b*) is 0.328 and that for the NES-less cylinder undergoing periodic VIV (figure 11*c*) is 0.212. The dramatic reduction in C_L can thus be directly attributed to the rotational NES. Along with the nearly 100 % reduction in the oscillation of C_D (figure 8*d*), this provides additional support for the hypothesis that the steady symmetric flow (with $C_L = 0$ and a steady C_D) is partially stabilized during each slowly decaying portion of the intermittently bursting solution.

For $\bar{r}_o = 0.5$, $\epsilon_p = 0.3$ and $\zeta_r = 0.340$, the time history of C_D during the slowly modulated response is shown in figure 8(*d*). A moving average of C_D continuously decreases during the slowly decaying portion of the solution, to a value of approximately 1.2 just before the chaotic transition, compared to a mean value of 1.85 for NES-less VIV. Equally significant, the oscillation amplitude of C_D decreases by nearly 100 %. These reductions in the mean value and oscillation amplitude C_D, both attributable to the rotational NES, further support our interpretation that the steady symmetric flow (with $C_D = 0.44$ close to the value at the Hopf bifurcation for the stationary cylinder) is partially stabilized during the slow decay part of the cycle.

From the time series of the cylinder and NES motions, and of C_L, along with the wake structure, one can associate the dynamics with relaxation oscillations punctuated by intermittent chaotic transitions during relaxation. Such relaxation oscillations can be attributed to TET from the vortical flow to the rectilinear cylinder motion to the rotational kinetic energy of the NES mass. Indeed, the NES continuously extracts kinetic energy from the flow and cylinder (dissipating it through its damper), thus

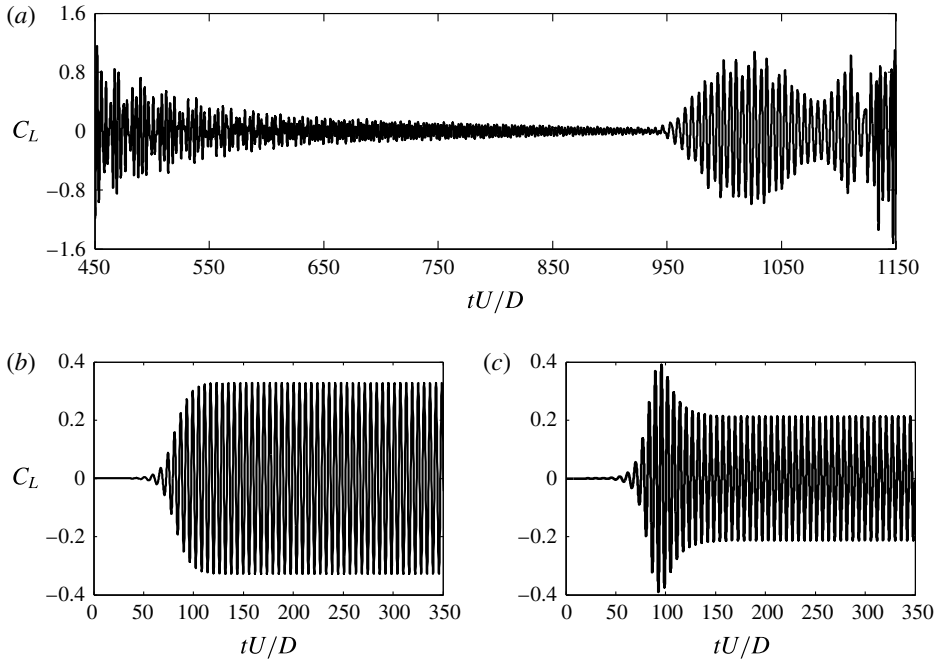

FIGURE 11. For $Re = 100$, lift coefficients (C_L) (*a*) with rotational NES ($\bar{r}_o = 0.5$, $\epsilon_p = 0.3$ and $\zeta_r = 0.340$); (*b*) stationary cylinder; and (*c*) cylinder undergoing standard VIV (without NES).

diminishing the VIV amplitude. Targeted energy transfer directed towards the NES not only reduces the amplitude of cylinder motion, but also provides a new dissipative mechanism (beyond viscosity in the flow) to suppress flow instability. It appears that this additional dissipation can, for certain combinations of the NES parameters, partially stabilize the steady symmetric flow. Beyond that, the results suggest that during the slow decay, a stage is reached in which cylinder motion increases more rapidly than can NES angular velocity or NES dissipation, resulting in destabilization of the low-amplitude, less unsteady flow, which in turn leads to sudden relaxation and transition into a chaotic large-amplitude, highly unsteady regime. The relaxation cycle then repeats itself after the NES angular velocity regains its capacity to extract energy from the flow, as described above.

4.3. *Existence of the elongated vortex over a range of parameters*

As we initially found the slowly decaying motion, its elongated attached vortex and significantly lower C_L and C_D coefficients, for only a single value of the parameters, the question naturally arises as to whether these features persist over a range of Re and NES parameters.

To gauge this persistence in the parameter space, we computed flows at $Re = 60$ with NES parameters different from those used at $Re = 100$. Since the Strouhal frequency varies with Re, we chose St at $Re = 60$ so that the parameters for the NES-less case can be tuned to the resonance condition in order to have large-amplitude oscillation of the cylinder. For a stationary cylinder at $Re = 60$ (for which $St = 0.14$), the time series of C_L and its frequency content are shown

in figures S2a and S2b in the supplementary material. Next, we tuned the natural frequency of the cylinder to be in resonance with the lift (at $f_n^* = St = 0.14$), and computed NES-less VIV to obtain the large-amplitude motion of the cylinder at $Re = 60$. The cylinder displacement and C_L at $Re = 60$ for NES-less VIV are shown in figures S3a and S3b, respectively, in the supplementary material.

We then introduced a rotational NES with $\bar{r}_o = 0.5$, $\epsilon_p = 0.3$, and $\zeta_r = 0.340$ (used at $Re = 100$), and found that the elongated region of attached vorticity is not observed at $Re = 60$. However, a coarse search shows that an elongated vortex solution exists for $Re = 60$ with $\bar{r}_o = 0.3$, $\epsilon_p = 0.3$ and $\zeta_r = 0.943$. The time series of the cylinder displacement, NES angle and lift coefficient are shown in figure 12(*a*,*b*,*d*), respectively. The angular velocity of the NES mass (figure 12*c*) shows that the NES mass changes direction frequently until a dimensionless time tU/D of approximately 450, and is unidirectional for $450 \leqslant tU/D \leqslant 620$. For $Re = 60$, the distribution of spanwise vorticity at $tU/D = 570$ (figure 12*e*) shows the elongated region of attached vorticity, at a time when the cylinder displacement (figure 12*a*) and lift coefficient (figure 12*d*) exhibit the typical scenario of chaotic bursting leading to slowly decaying motion of the cylinder and a very small C_L. However, there are clear differences between the responses at $Re = 60$ and 100 (see figure 8). The magnitude of C_L is much smaller at $Re = 60$, which is expected since $Re = 60$ is closer to the Hopf bifurcation that occurs near $Re = 46$. The intervals during which the cylinder motion is chaotic and in the slowly decaying regime are much shorter at $Re = 60$ than at $Re = 100$. As Re is reduced from 100 to 60, we expect that damping provided by the flow will increase due to increased viscous dissipation, resulting in shorter durations of the chaotic and slow decay regimes.

Near $Re = 100$, $f_n^* = 0.167$, $\bar{r}_o = 0.5$, $\epsilon_p = 0.3$ and $\zeta_r = 0.340$ (the parameters for which an elongated vortex was originally found), we consider persistence of the elongated vortex solution for small changes in Re and the NES parameters. To determine the dependence of the solution and the elongated vortex structure on Re near 100, we perform a survey over the range $95 \leqslant Re \leqslant 105$ with a unit increment, using the nominal values of f_n^* and the rotational NES parameters. Figure 13(*a*,*b*) shows that disturbances grow very slowly until a dimensionless time of just less than $tU/D = 100$, at which point rapid amplification occurs. The time of onset for rapid amplification decreases slightly with increasing Re. For each Re shown, rapid amplification gives rise to a second, temporally chaotic, transient whose duration varies from approximately 500 convective time units (at $Re = 95$) to approximately 100 time units (at $Re = 101$). For $Re < 100$, figure 13(*a*,*b*) shows that this second transient ultimately settles down to a time-periodic solution, whereas for $Re > 100$, figure 13(*c*,*d*) shows that the second transient is followed by slow decay until bursting occurs. For $f_n^* = 0.167$, $\bar{r}_o = 0.5$, $\epsilon_p = 0.3$ and $\zeta_r = 0.340$, we do not find the elongated wake solution for $Re < 100$, the range of Re for which the time series of cylinder displacement shows no slow decay. For $Re \geqslant 100$, an elongated vortex is found. Figure 13(*e*,*f*) shows the elongated wake structure at its maximum extent during the slowly decaying portion of the cylinder displacement time series at $Re = 101$ and $Re = 105$, respectively.

The effect on the elongated vortex structure of changing the relative mass of the NES is shown in figure 14. When ϵ_p is reduced to 0.28, the elongated vortex solution is still found, with the cylinder displacement and spanwise vorticity shown in figure 14(*a*,*c*), respectively. The cylinder displacement and spanwise vorticity for $\epsilon_p = 0.35$ are shown in figure 14(*b*,*d*), respectively. For the lighter NES mass, the slowly decaying envelope extends over a longer time. In addition, the decay does not have the typical linear envelope found in other cases.

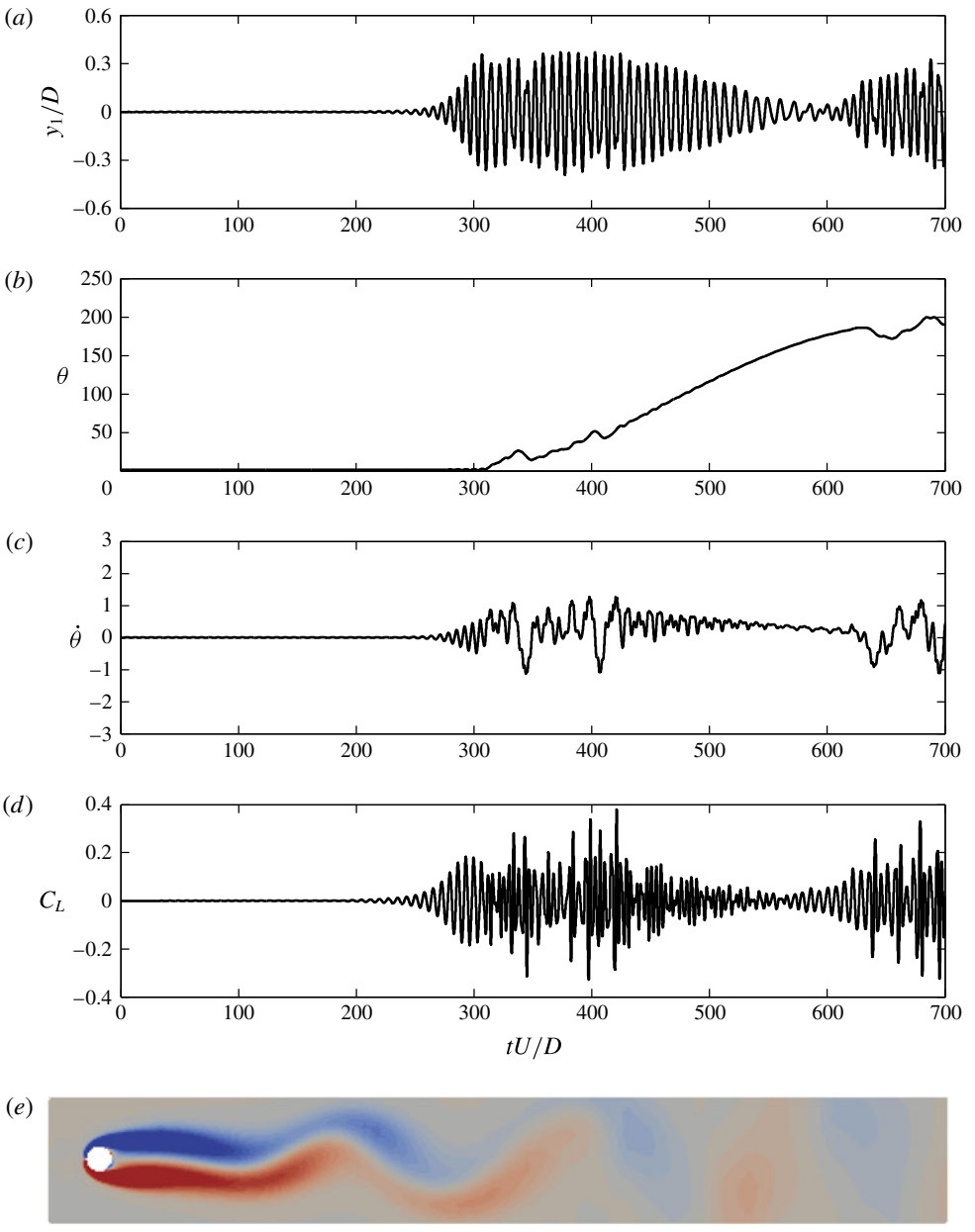

FIGURE 12. (Colour online) Response at $Re = 60$ and $f_n^* = 0.14$ for $\bar{r}_o = 0.3$, $\epsilon_p = 0.3$ and $\zeta_r = 0.943$. (*a*) Cylinder displacement (Y_1); (*b*) NES angle (θ); (*c*) NES angular velocity ($\dot{\theta}$); (*d*) lift coefficient (C_L); and (*e*) spanwise vorticity (ω).

The elongated vortex has been found over a significant range of the NES damping parameter ζ_r. For $\zeta_r = 0.255$ and 1.698, time series of cylinder displacement shown in figure 15(*a*,*b*) indicate that for the larger ζ_r, the slowly decaying portion of the solution (approximately $250 \leqslant tU/D \leqslant 370$) is considerably shorter than for the smaller ζ_r (approximately $180 \leqslant tU/D \leqslant 800$), and also accounts for a smaller fraction of the

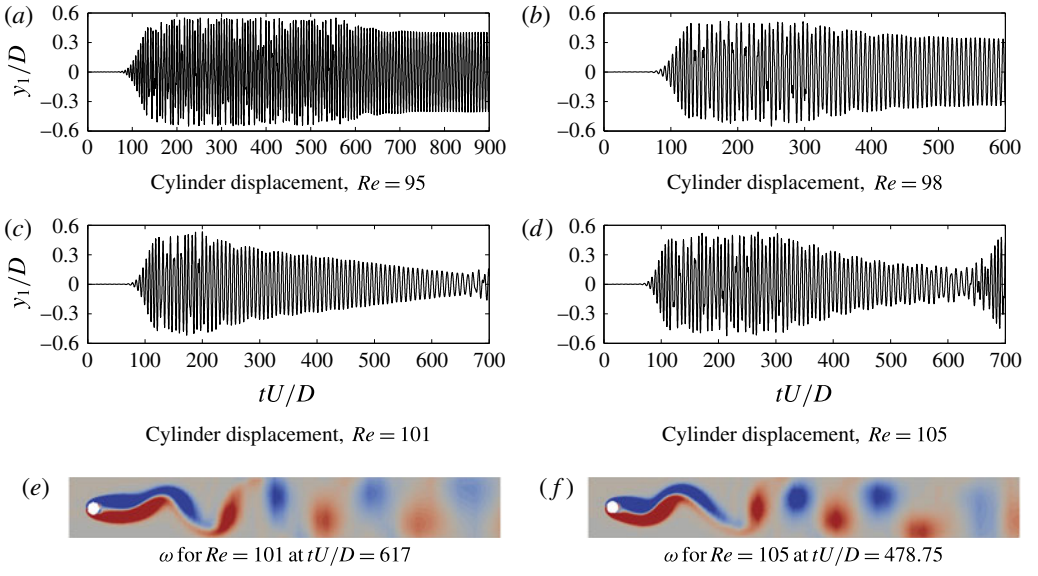

FIGURE 13. (Colour online) Persistence of elongated wake solution for small changes in Re with $\bar{r}_o = 0.5$, $\epsilon_p = 0.3$ and $\zeta_r = 0.340$.

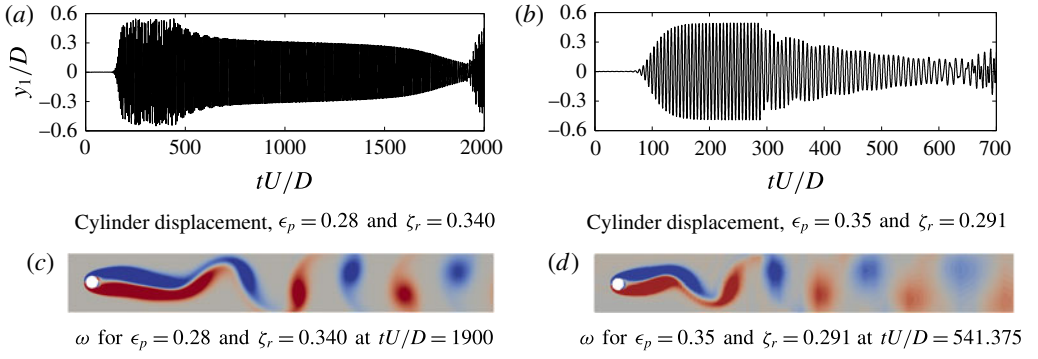

FIGURE 14. (Colour online) Persistence of elongated wake solution as ϵ_p and ζ_r vary, with $Re = 100$ and $\bar{r}_o = 0.5$.

overall cycle. Figure 15(*c*,*d*) shows that the elongated vortex is quite similar for these two ζ_r, even though the time series of cylinder displacement are quite different. The slower decay in cylinder displacement at the smaller ζ_r is consistent with reduced dissipation by the NES of energy transferred from the flow to the cylinder motion.

The effect of radius of the rotating NES mass on the elongated wake solution is shown in figure 16. Figure 16(*b*) shows that the elongated vortex persists down to $\bar{r}_o = 0.47$. We note that the slowly decaying envelope of the cylinder displacement shown in figure 16(*a*) with $\bar{r}_o = 0.47$ is very similar to that for the lower mass case ($\epsilon_p = 0.28$) shown in figure 14(*a*).

These results show that for $m^* = 10$ and $f_n^* = 0.167$, the elongated attached vortex exists over a range of Re and NES parameters.

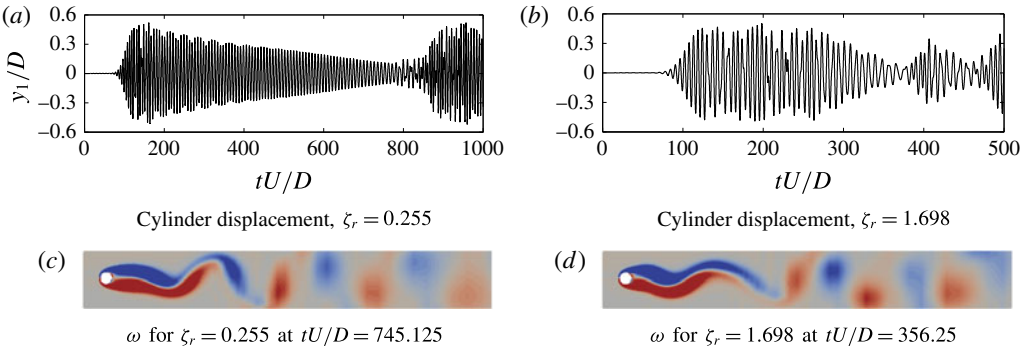

FIGURE 15. (Colour online) Persistence of elongated wake solution for two values of ζ_r, with $Re = 100$, $\bar{r}_o = 0.5$ and $\epsilon_p = 0.3$.

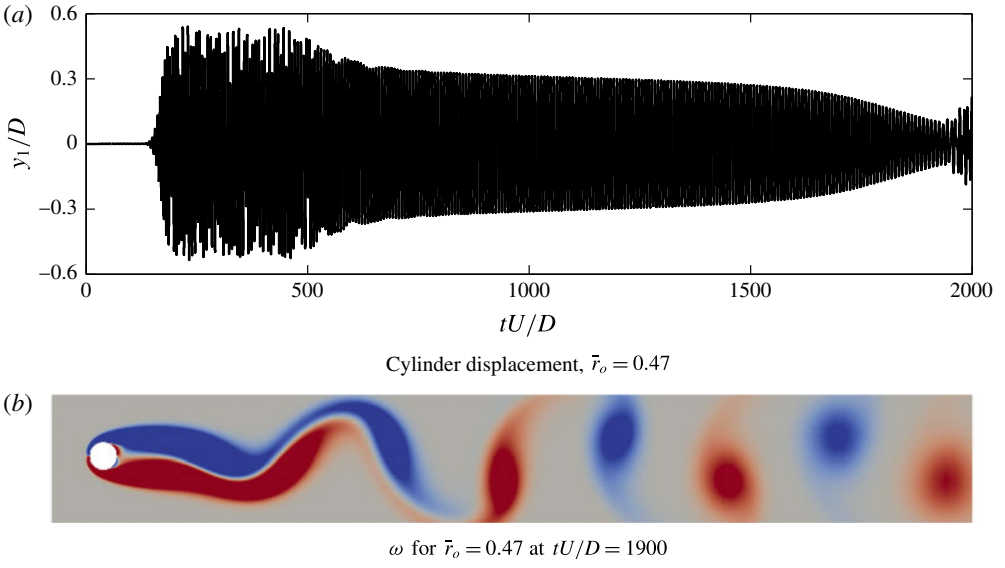

FIGURE 16. (Colour online) Persistence of elongated wake solution for a small change in $\bar{r}_o$ with $Re = 100$, $\epsilon_p = 0.3$ and $\zeta_r = 0.340$.

In addition to the NES parameters and Re, we also show that the elongated vortex solution persists for changes in initial conditions. For this case, we initially 'lock' the NES mass, so that there is no NES motion during an initial transient. Since the NES mass is a fixed fraction of the cylinder mass, the combined mass of the system remains the same as for the system without the NES. Thus, standard VIV at $Re = 100$ is expected with the NES mass locked. (The cylinder does not rotate, so if it is rigid, the non-axisymmetric distribution of the internal mass due to the NES has no effect.) After the standard VIV solution is fully developed, the NES is set free, with a displacement of $\theta = \pi/2$, to interact with the stator and flow. The results are shown in figure 17, where the NES mass is locked until $tU/D = 288$, at which time VIV is fully developed, with maximum cylinder amplitude $y_1/D = 0.49$ and maximum lift coefficient $C_L = 0.212$, as for the system without an NES. Beyond $tU/D = 288$, figure 17(*a*) shows that the system enters into exactly the same response as shown

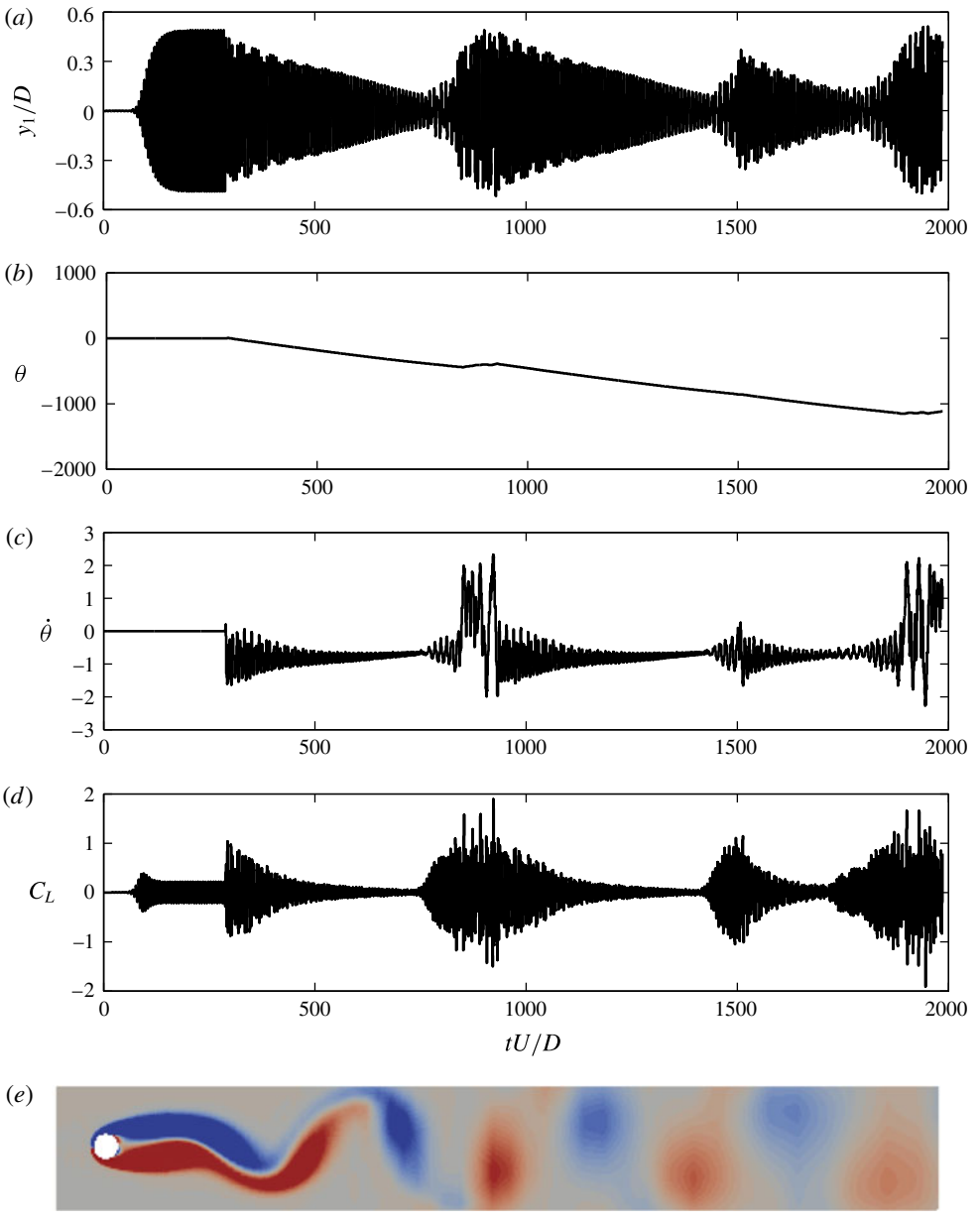

FIGURE 17. (Colour online) Response at $Re = 100$ for $\bar{r}_o = 0.5$, $\epsilon_p = 0.3$ and $\zeta_r = 0.340$ for cylinder with NES locked until $tU/D = 288$ and released at that time with $\theta = \pi/2$. (*a*) Cylinder displacement (Y_1); (*b*) NES angle (θ); (*c*) NES angular velocity ($\dot{\theta}$); (*d*) lift coefficient (C_L); and (*e*) spanwise vorticity (ω) at $tU/D = 710.375$.

in figure 8(*a*). The distribution of spanwise vorticity at $tU/D = 710.375$ (figure 17*e*) shows that the elongated vortex develops from the standard VIV solution just as it does from the usual initial condition.

5. Characterization of the chaotic response

Quasi-periodicity and temporal chaos (collectively, 'temporal complexity') in the wake of a circular cylinder at low Re (say, below $Re = 100$) has been of interest since the initial report by Sreenivasan (1985). The careful experiments of Van Atta & Gharib (1987) showed that wake characteristics depended sensitively on tension in the wire used as the cylinder, and that damping of wire motion (beyond test section sidewalls) sometimes eliminated temporal complexity. On the other hand, in two definitive series of experiments in Sreenivasan's laboratory, Olinger (1993) showed that chaotic response at Re as low as 59 is sometimes uncoupled from VIV. In one series, he varied wire tension, which affected the natural frequency, but did not affect the wake hot-wire signal at frequencies associated with shedding. (Cylinder vibration in Olinger's work had a natural frequency less than the shedding frequency, whereas in Van Atta and Gharib's experiments, cylinder vibration was predominately at a harmonic of the natural frequency, above the Strouhal frequency.) From this, Olinger concluded that in his facility, chaotic response at low Re could result from interaction of three incommensurate frequencies, associated with (i) nominally two-dimensional Kármán vortex shedding, (ii) a spanwise non-uniform cellular structure and (iii) end-plate effects, and that VIV was not necessary to the explanation. In the other series, Olinger measured wire displacement with a laser vibrometer and found the response to be nearly identical for temporally complex flow, and for no flow. With flow, driven by pumps one story below the wind tunnel, cylinder motion was essentially the same as when the pumps ran but there was no flow. That provided strong support for the conclusion that for those cylinders in that facility, cylinder motion was driven by extrinsic vibration.

Of the other investigations reporting temporal complexity in flow past a vibrating circular cylinder at low Re, each has either involved end effects (Dauchy, Dušsek & Fraunié 1997) or forced periodic excitation (Olinger & Sreenivasan 1988; Li, Sun & Roux 1992; Nakano & Rockwell 1994; Anagnostopoulos 2000*a*,*b*), or an empirical structural damping parameter was used at an Re considerably larger than the values at which we find chaotic response (250 for Blackburn & Henderson (1996); 200 for Leontini *et al.* (2006)).

The significance of the lower Re (60 and 100) at which we have found a two-dimensional temporally chaotic flow, compared to the value of 200 of Leontini *et al.* (2006), is that it establishes the existence of chaotic response at Re values well removed from those at which Leontini *et al.* (2007) found three-dimensional instability in the two-dimensional base flow past a cylinder undergoing driven harmonic transverse oscillation ($Re = 205$), and at which Williamson (1988) found three-dimensional disturbances to become unstable for a fixed cylinder ($Re = 190$).

Here, we focus on several measures of temporal chaos, including the attractor dimension of the cylinder velocity and the cross-stream and streamwise components of the fluid velocity at several locations, as well as wavelet transformations of the same quantities. We also present results of cross-correlation of the cylinder velocity with each velocity component of the flow at several points.

For $Re = 100$, $\bar{r}_o = 0.5$, $\epsilon_p = 0.3$ and $\zeta_r = 0.340$ (the case shown in figure 8), figure 18(*a*) shows the cylinder velocity during the chaotic portion of the response, while the frequency content revealed by WT and 'fast Fourier transform' (FFT) is shown in figure 18(*c*,*e*), respectively. By comparison, the cylinder velocity for NES-less periodic VIV at $Re = 100$ is shown in figure 18(*b*), and its WT and FFT are shown in figure 18(*d*,*f*), respectively. The broadband frequency content for the system with an NES demonstrates the chaotic nature of the cylinder motion during this time

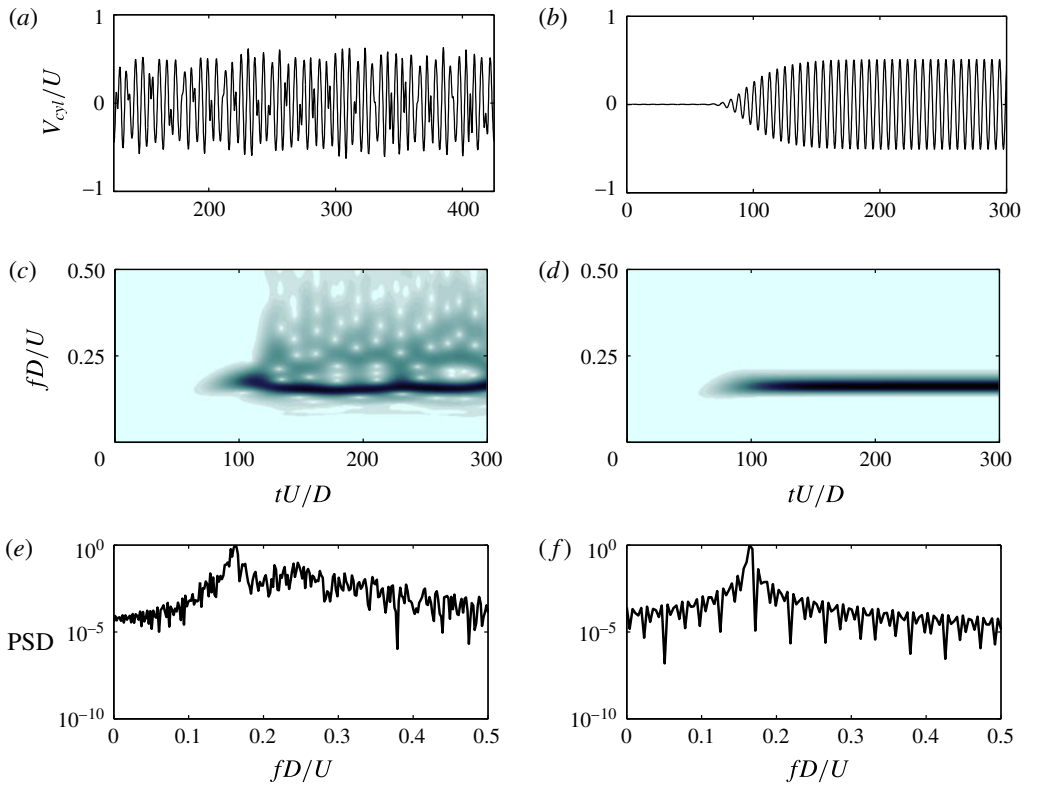

FIGURE 18. (Colour online) Cylinder velocity at $Re = 100$. Chaotic response with NES (a,c,e) for $\bar{r}_o = 0.5$, $\epsilon_p = 0.3$ and $\zeta_r = 0.340$, and periodic response system without NES (b,d,f). (a) Cylinder velocity with NES; (b) cylinder velocity without NES; (c) WT of cylinder velocity with NES; (d) WT of cylinder velocity without NES; (e) FFT of cylinder velocity with NES; (f) FFT of cylinder velocity without NES.

interval, whereas the periodic solution has a single dominant frequency close to the Strouhal frequency, as expected.

We next examine the flow during the chaotic response, by considering the velocity at two fixed locations in the wake. The first is one diameter above the midline of the domain and one diameter downstream of the rear of the cylinder. By comparison, for the periodic solution in the NES-less standard VIV case at $Re = 100$, the streamwise velocity component in an inertial frame and its frequency content obtained by WT and FFT, are shown in figure 19(a,c,e), with the corresponding quantities for the cross-stream component in figure 19(b,d,f), respectively. The WT and FFT clearly show a dominant frequency, indicating the periodic nature of the flow in the wake.

The cross-correlations of the cylinder velocity with the streamwise and cross-stream velocity components are calculated as

$$a_u(\tau_c) = \frac{1}{U^2(T_2 - T_1)} \int_{T_1}^{T_2} V_{cyl}(t) u(x_p, y_p, t + \tau_c)\, \mathrm{d}t, \tag{5.1a}$$

$$a_v(\tau_c) = \frac{1}{U^2(T_2 - T_1)} \int_{T_1}^{T_2} V_{cyl}(t) v(x_p, y_p, t + \tau_c)\, \mathrm{d}t, \tag{5.1b}$$

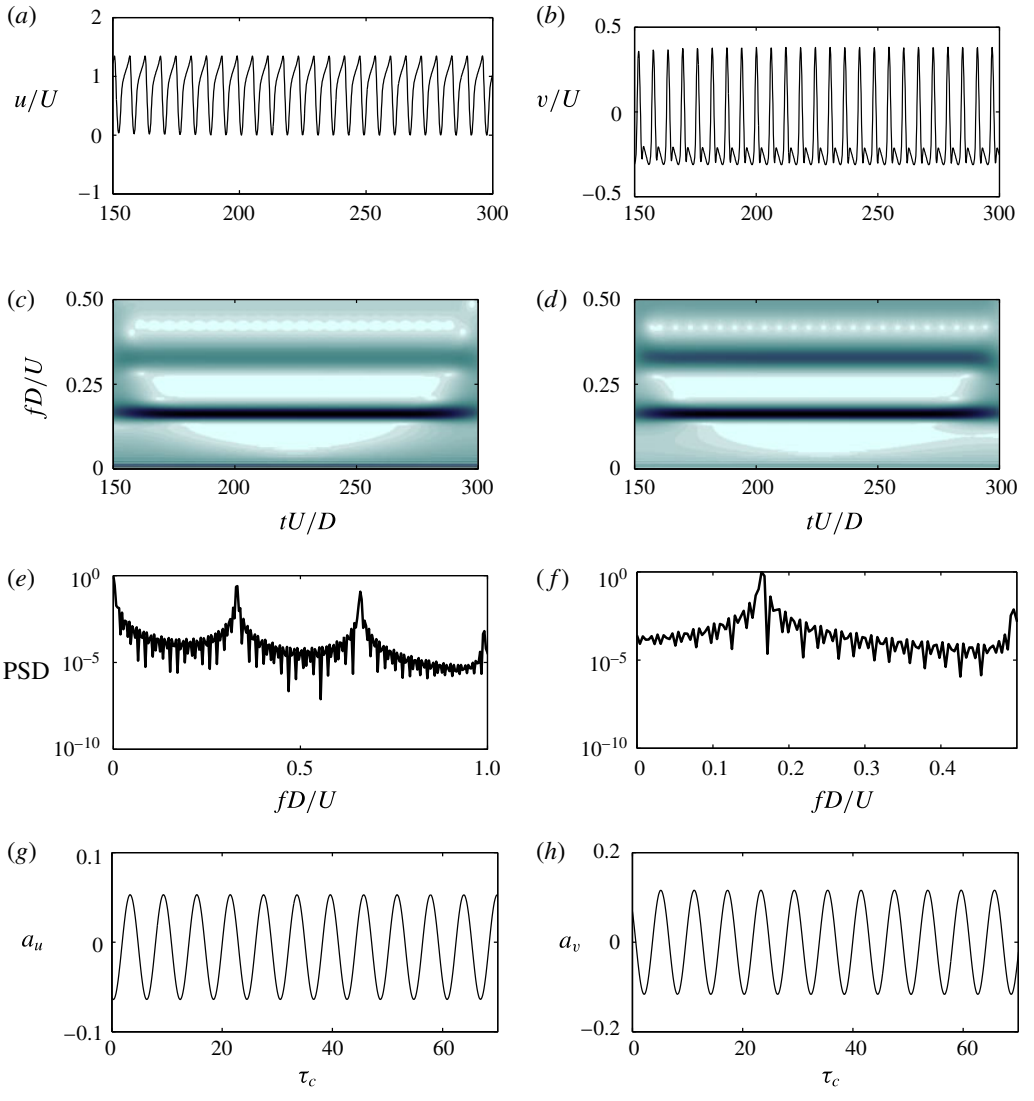

FIGURE 19. (Colour online) For NES-less VIV at $Re = 100$, periodic nature of the flow at a fixed point one diameter downstream of rear stagnation point and one diameter from $y = 0$. (*a*) Streamwise velocity; (*b*) cross-stream velocity; (*c*) WT of streamwise velocity; (*d*) WT of cross-stream velocity; (*e*) FFT of streamwise velocity; (*f*) FFT of cross-stream velocity; (*g*) streamwise velocity cross-correlation with cylinder velocity; (*h*) cross-stream velocity cross-correlation with cylinder velocity.

and are shown in figure 19(*g*,*h*) for the streamwise and cross-stream velocity, respectively, with $T_1 = 150$ and $T_2 = 275$. Both cross-correlations are periodic, as one would expect for a periodic flow.

For the case with a rotational NES undergoing chaotic cylinder motion, the fluid velocity one diameter above the midline and one diameter downstream of the rear of the cylinder are shown in figure 20(*a*,*b*) for the streamwise and cross-stream components, respectively. The frequency content obtained via WT and FFT is shown

in figure 20(*c*,*e*), respectively, for the streamwise component and in figure 20(*d*,*f*), respectively, for the cross-stream component. As for the cylinder motion, the chaotic nature of the flow in the near wake can be discerned from the frequency content, and by comparison to the periodic case shown in figure 19. For the chaotic solution, the cross-correlations of the cylinder velocity are shown in figure 20(*g*,*h*) for the streamwise and cross-stream velocity components, respectively, with $T_1 = 125$ and $T_2 = 700$. The cross-correlation decays with time for both velocity components, and strongly suggests the chaotic nature of the flow at $Re = 100$ when the rotational NES is active. Very similar results are found at the second location, three diameters downstream of the rear of the cylinder and one diameter above the midline of the domain.

To complement the frequency spectra and autocorrelation functions, we estimate the correlation dimension of the chaotic attractor. We use the algorithm of Grassberger & Procaccia (1983), and apply the code developed by Hegger, Kantz & Schreiber (1999) to the cylinder displacement time series shown in figure 8(*a*), with logarithmic plots of the correlation dimension $C_m(\sigma)$ versus the 'distance' σ shown in figures S4(a–f) in the supplementary material for six values of the embedding dimension m, using approximately 300 points per quasi-period, a time delay corresponding to 60 sampled points, and a Theiler window parameter corresponding to 800 sampled points.

The results, along with least-squares lines fitted over the indicated range of σ, show that the slope (corresponding to the correlation dimension) approaches a limiting value of approximately 3.2. This value is consistent with a low-dimensional attractor expected for a low-*Re* flow with two additional degrees of freedom (the cylinder oscillation and NES rotation), and is comparable to the fractal dimensions of 2.48, 3.10 and 4.65 computed for chaotic two-dimensional flow past a NACA 0012 airfoil ($Ma = 0.2$; 20° angle of attack) at $Re = 1600$, 2000 and 3000, respectively (Pulliam & Vastano 1993).

It is thus clear that a rotational NES can lead to temporal chaos of the cylinder motion and the flow, at Reynolds numbers where NES-less VIV is strictly time periodic.

6. Discussion

6.1. *NES-induced effective mass model*

Equation (2.2*a*) shows that the cylinder motion is driven by the oscillating lift force and the essentially nonlinear coupling to the NES. Consider the latter term

$$N = \hat{M}_{rnes} r_o \frac{\mathrm{d}}{\mathrm{d}t}\left(\frac{\mathrm{d}\theta}{\mathrm{d}t}\sin\theta\right). \tag{6.1}$$

Interaction of the rotational NES with the flow, mediated by the cylinder, can be approximated by adding to the cylinder a time-varying NES-induced effective mass (per unit length), which we define as the ratio of the nonlinear restoring force (per unit length) to the acceleration of the cylinder, $\hat{M}_{eff}(t) = -N(t)/(\mathrm{d}^2y/\mathrm{d}t^2)$. In dimensionless form, this is

$$m_{eff} = -\frac{\epsilon_p \bar{r}_o}{\ddot{Y}_1}\frac{\mathrm{d}}{\mathrm{d}\tau}\left(\frac{\mathrm{d}\theta}{\mathrm{d}\tau}\sin\theta\right). \tag{6.2}$$

For $Re = 100$, $\bar{r}_o = 0.5$, $\epsilon_p = 0.3$ and $\zeta_r = 0.340$, figure 21(*a*) shows m_{eff} for four time intervals during which the NES locks into a slowly decaying motion. Since m_{eff}

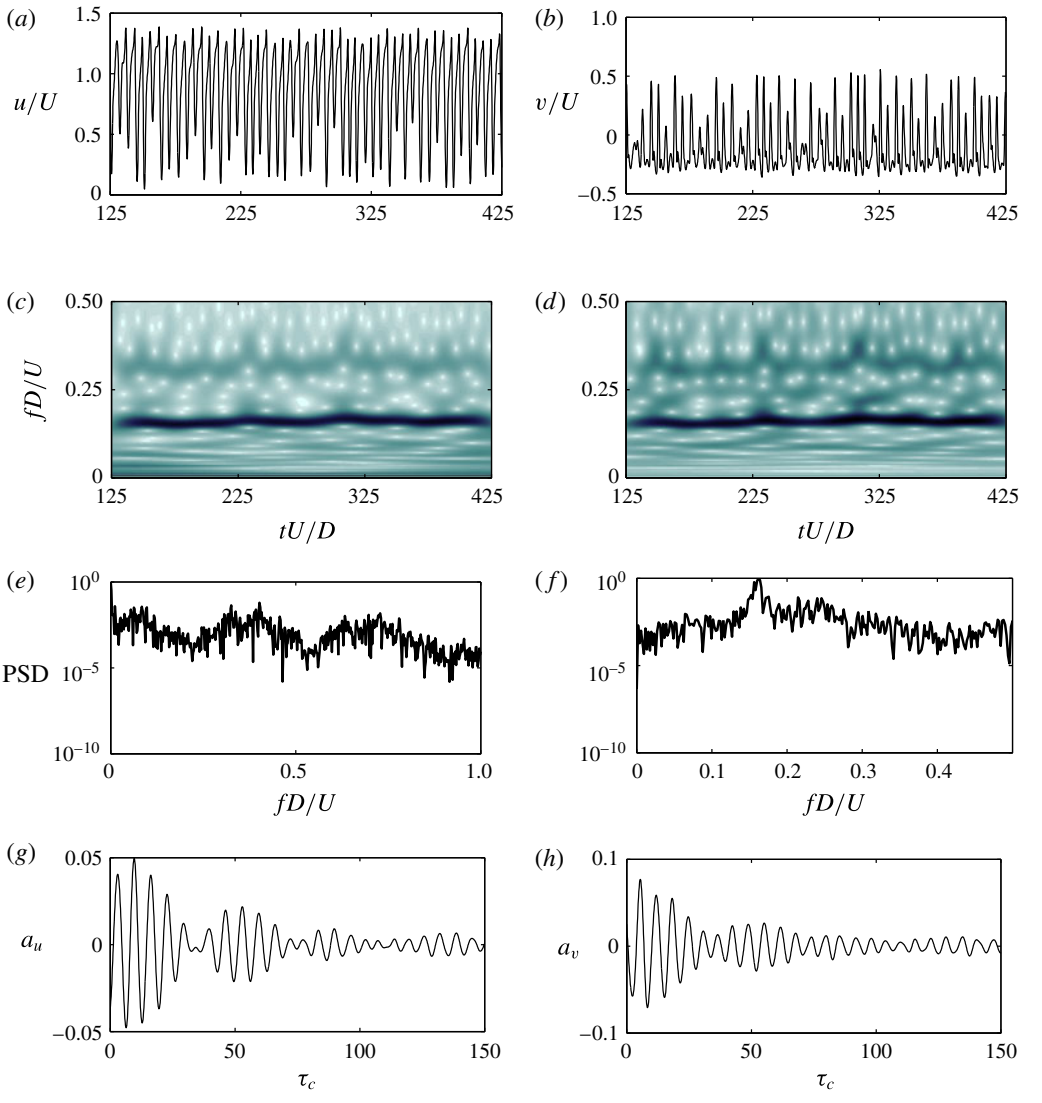

FIGURE 20. (Colour online) For VIV at $Re = 100$, $\bar{r}_o = 0.5$, $\epsilon_p = 0.3$ and $\zeta_r = 0.340$, chaotic nature of the flow at a fixed point one diameter downstream of rear stagnation point and one diameter from $y = 0$. (*a*) Streamwise velocity; (*b*) cross-stream velocity; (*c*) WT of streamwise velocity; (*d*) WT of cross-stream velocity; (*e*) FFT of streamwise velocity; (*f*) FFT of cross-stream velocity; (*g*) streamwise velocity cross-correlation with cylinder velocity; (*h*) cross-stream velocity cross-correlation with cylinder velocity.

is the quotient of two quantities each oscillating about zero, the result will include singularities that we filter out by Gaussian smoothing (Harris 1978). In each portion of the time series shown separately in figure 21(*a*), m_{eff} approaches unity toward the end of the decaying motion, i.e. the NES-induced effective mass is as large as the mass of the cylinder and NES. Addition of this dynamic mass to the cylinder mass also explains the large frequency detuning near the end of each slowly decaying motion. The natural frequency of the structural system, including the effective NES-induced

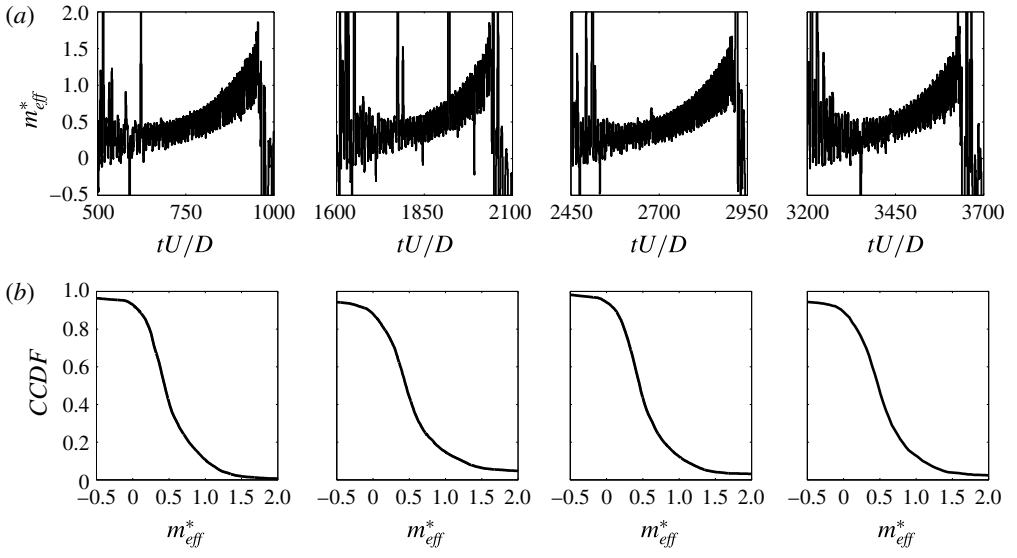

FIGURE 21. For $Re = 100$, $\bar{r}_o = 0.5$, $\epsilon_p = 0.3$ and $\zeta_r = 0.340$, (*a*) dimensionless NES-induced effective mass for four time intervals and (*b*) corresponding complementary cumulative distribution functions (*CCDF*).

mass, is $\omega_{detuned} = \omega_r^*/\sqrt{2}$. Hence, doubling the mass reduces the frequency to $1/\sqrt{2} \approx 70\,\%$ of its original value, which closely corresponds to the 33 % frequency detuning found in the cylinder response near the end of each slow decay.

For each time interval during which the NES locks into slowly decaying motion, figure 21(*b*) shows the complementary cumulative distribution function (*CCDF*) of the effective mass induced by the NES. The *CCDF* plots indicate that the probability of mass being additive in this response is high, since $CCDF(m_{eff} = 0) \approx 0.95$ in all such time intervals. In contrast, for the passive suppression Mechanisms I and II discussed in § 4.1, where no elongated vortex structure is found, figure 22(*a*,*b*) shows that there is no overall trend in the mean value of m_{eff}, and the lock-in response in these cases occurs with a frequency close to the Strouhal frequency. The *CCDF* of the effective NES-induced mass for these two mechanisms is shown in figure 22(*c*,*d*), from which we deduce that m_{eff} fluctuates about a zero mean, corresponding to no effective added mass, with $CCDF(m_{eff} = 0) \approx 0.35$ and 0.4 for Mechanisms I and II, respectively.

These results strongly suggest (but do not prove) that the increase in NES-induced mass is related to changes in vortex structure for the intermittently bursting solution.

6.2. *Approximate analysis of cylinder motion during the slowly modulated solution*

In this section, we perform an approximate analysis of cylinder motion during the slowly decaying motion discussed in § 4.2, in order to show that during the slowly decaying motion giving rise to the elongated vortex structure, the effect of the flow on cylinder motion is in its effect similar to linear viscous dissipation. With this analysis, we correlate the observed NES-induced effective mass and the computed frequency detuning. To this end, we consider the system of equations governing the coupled motion of the cylinder and NES

$$\frac{\mathrm{d}^2 Y_1}{\mathrm{d}\tau^2} + \omega_r^{*2} Y_1 = \epsilon_p \bar{r}_o \frac{\mathrm{d}}{\mathrm{d}\tau}\left(\frac{\mathrm{d}\theta}{\mathrm{d}\tau}\sin\theta\right), \tag{6.3a}$$

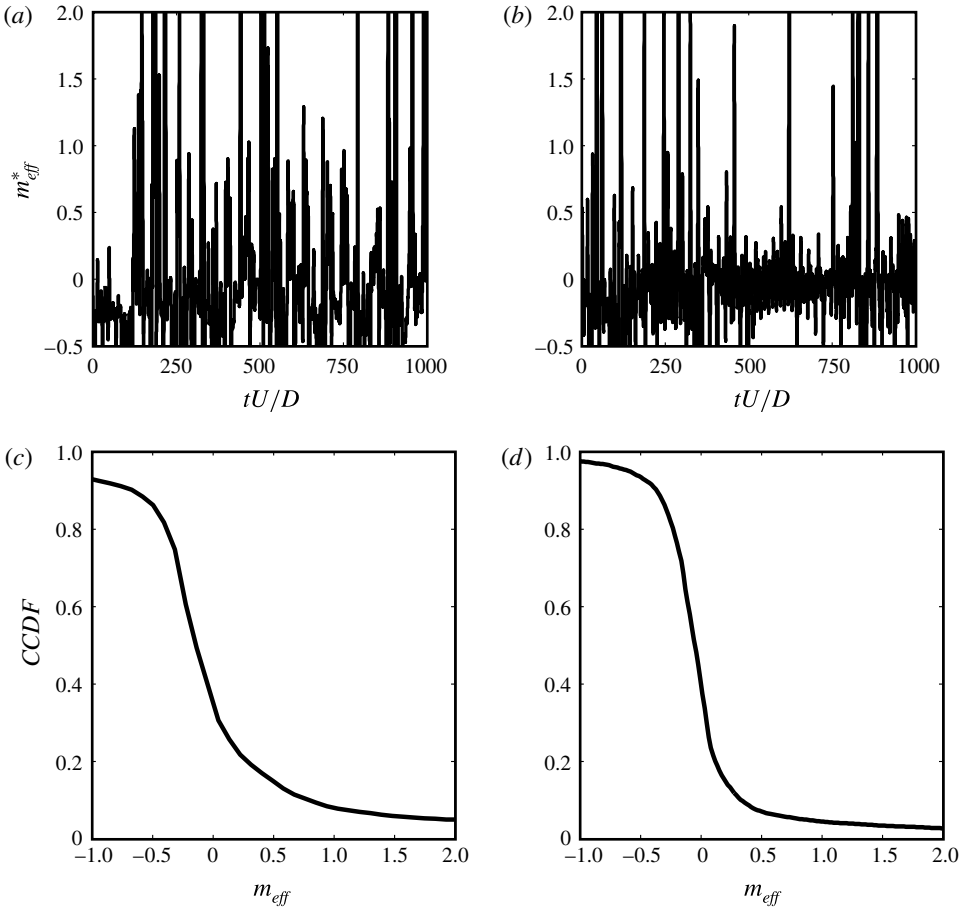

FIGURE 22. For $Re = 100$, dimensionless effective NES-induced mass for (*a*) Mechanism I (for $\bar{r}_o = 0.2$, $\epsilon_p = 0.3$ and $\zeta_r = 21.221$) and (*b*) Mechanism II (for $\bar{r}_o = 0.2$, $\epsilon_p = 0.25$ and $\zeta_r = 98.40$) and *CCDF* of effective NES-induced mass for Mechanisms I (*c*) and II (*d*).

$$\frac{\mathrm{d}^2\theta}{\mathrm{d}\tau^2} + \frac{\zeta_r}{Re}\frac{\mathrm{d}\theta}{\mathrm{d}\tau} = \frac{\mathrm{d}^2 Y_1}{\mathrm{d}\tau^2}\frac{\sin\theta}{\bar{r}_o} \tag{6.3b}$$

decoupled from the flow, where $\omega^*_r = 2\pi f^*_n$.

For $Re = 100$, $\bar{r}_o = 0.5$, $\epsilon_p = 0.3$ and $\zeta_r = 0.340$, the ordinary differential equations (ODEs) (6.3*a*) and (6.3*b*), subject to initial conditions taken from discretization of the partial differential equations (PDEs) and other equations of the fully coupled system at the beginning of the slowly decaying motion (namely $Y_1(550) = -0.309623$, $\mathrm{d}Y_1(550)/\mathrm{d}\tau = -0.028324$, $\theta(550) = 90.935038$ and $\mathrm{d}\theta(550)/\mathrm{d}\tau = 1.167909$) were solved using the MATLAB ODE45 solver. The cylinder displacement and NES mass angular displacement predicted by (6.3*a*) and (6.3*b*) are compared to the corresponding results for the PDE solution in figure 23(*a*,*b*), and figure 23(*c*,*d*), respectively. Equations (6.3*a*) and (6.3*b*), with initial conditions taken from the discretized PDE solution, provide qualitatively correct predictions of the slow decay of the cylinder displacement and unidirectional NES mass rotation. One apparent

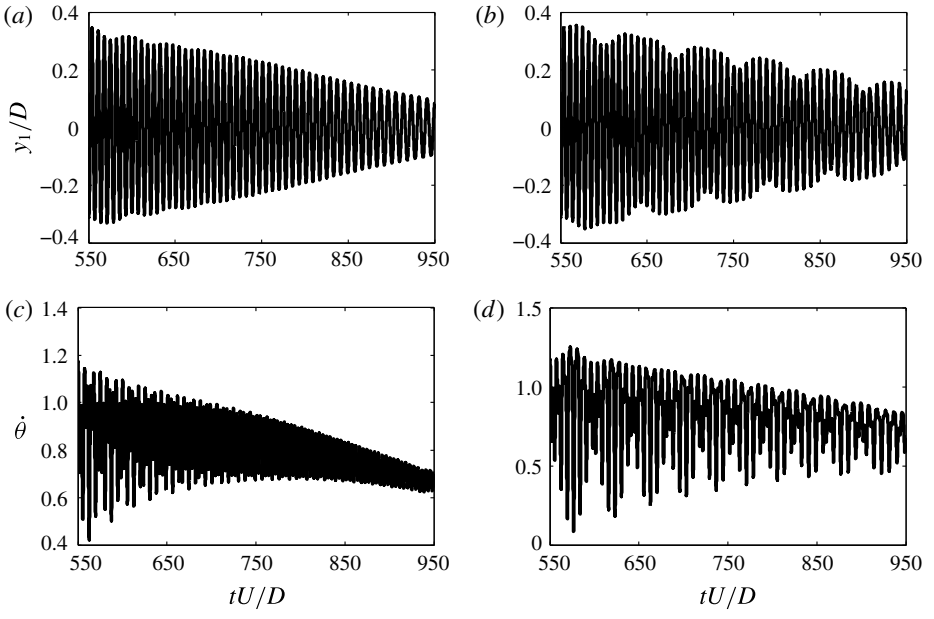

FIGURE 23. For $Re = 100$, $\bar{r}_o = 0.5$, $\epsilon_p = 0.3$ and $\zeta_r = 0.340$, solution of full, PDE-based equations compared to solution of unforced ordinary differential equation (ODE) system using initial conditions from PDE solution. (*a*) Cylinder displacement from PDE; (*b*) cylinder displacement from ODE; (*c*) NES angular velocity from PDE; (*d*) NES angular velocity from ODE.

difference is modulation in the slowly decaying envelope predicted by the ODE model. It will be shown later in this section that this additional modulation is due to omission of the flow from (6.3*a*) and (6.3*b*), which contributes to additional damping of the system.

Based on the solution of the ODE system (6.3*a*) and (6.3*b*), we conjecture that the slow modulation response is a dissipative perturbation of the solution of the underlying Hamiltonian system, which we approximate by neglecting damping of NES rotation in (6.3*b*). Assuming harmonic cylinder motion and unidirectional NES rotation, we approximate the response according to the ansatz $\tilde{Y}_1 = \bar{r}_o \alpha \cos \omega\tau$, $\tilde{\theta} = \omega\tau$, where the amplitude α and frequency ω are assumed to vary on a time scale slower than τ. Substituting into (6.3*a*) and (6.3*b*), with $\zeta_r = 0$, gives the frequency–amplitude relation

$$\alpha = \frac{\epsilon_p \omega^2}{\omega_r^{*2} - \omega^2}. \tag{6.4}$$

We can then evaluate (6.4) near the beginning (at τ_1) and end (at τ_2) of a slowly decaying portion of the time series, and eliminate ω_r^{*2} to get

$$\frac{\omega_2}{\omega_1} = \sqrt{\frac{\alpha_2 \left(\alpha_1 + \epsilon_p\right)}{\alpha_1 \left(\alpha_2 + \epsilon_p\right)}}. \tag{6.5}$$

Substituting cylinder displacement amplitudes from the PDE solution into (6.5), we obtain the analytical estimate $\omega_2/\omega_1 = 0.777$ for the portion of the time series shown

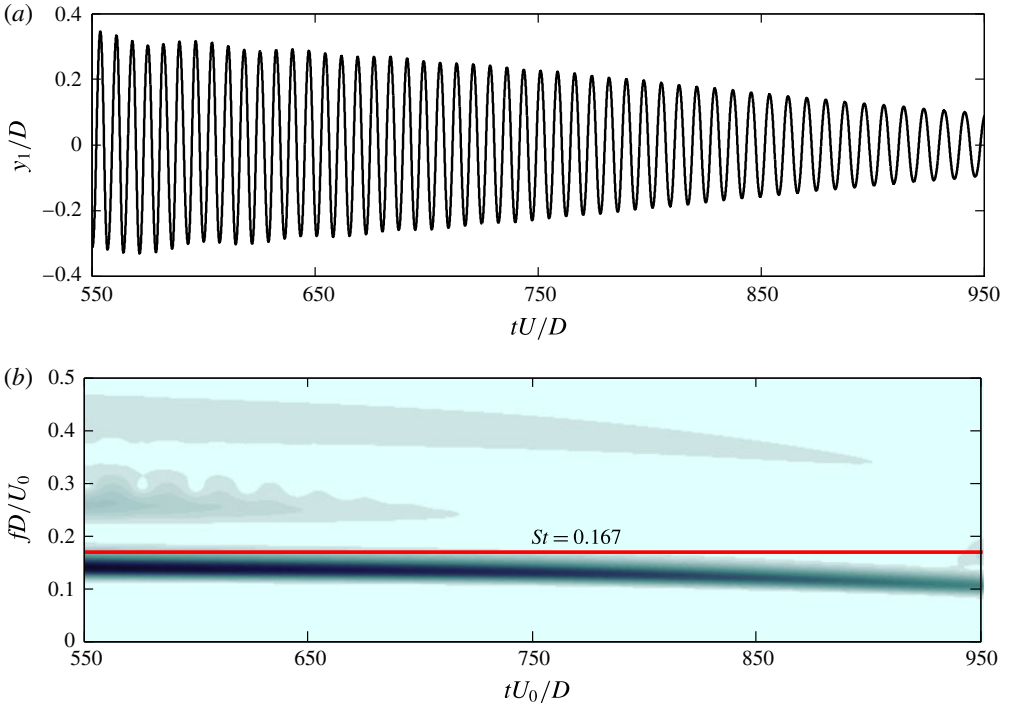

FIGURE 24. (Colour online) For $Re = 100$, $\bar{r}_o = 0.5$, $\epsilon_p = 0.3$ and $\zeta_r = 0.340$, frequency detuning in one slow modulation portion of the solution. (*a*) Cylinder displacement and (*b*) frequency of cylinder displacement.

in figure 24(*a*). The frequency content of the solution of the full PDE system is extracted by taking a wavelet transform of the cylinder displacement for $550 \leqslant tU/D \leqslant 950$, shown in figure 24(*b*). The frequency ratio from the PDE solution is found to be $\omega_2/\omega_1 = 0.789$. The good agreement between the frequency ratios obtained from the approximate model (6.5) and the PDE solution supports our conjecture that the observed slow modulation cycle is a perturbation of the underlying undamped system.

At the beginning of the slowly decaying response, the results show that no *ad hoc* damping is necessary to achieve qualitative agreement with the PDE model. In a sense, the cylinder motion reaches, via a chaotic transition, a state where no coupling to the flow is necessary. This might suggest that as the amplitude of the cylinder motion decreases, the behaviour of the overall system (as described by the PDEs coupled to the rigid-body dynamics) approaches that of a fixed cylinder, since the amplitude of the cylinder oscillation is well below that for standard VIV at the same Re, m^* and f_n^*. That this is not the case is seen from the elongation of the attached vorticity in figure 10(*a*), which does not correspond to flow past a fixed cylinder. Rather, the overall system behaviour is partially stabilized and approaches (but does not reach) that of the SSMC flow. In that limit, there is no lift, and hence no cylinder motion, and so as one approaches that limit, the interaction of the flow with the cylinder is indeed expected to be weak. We attribute the elongated vortex flow to the existence of a state in which the energy transfer rate from the flow to the cylinder is nearly balanced dynamically (as opposed to over one oscillation period) by the rate at which energy is dissipated by the NES.

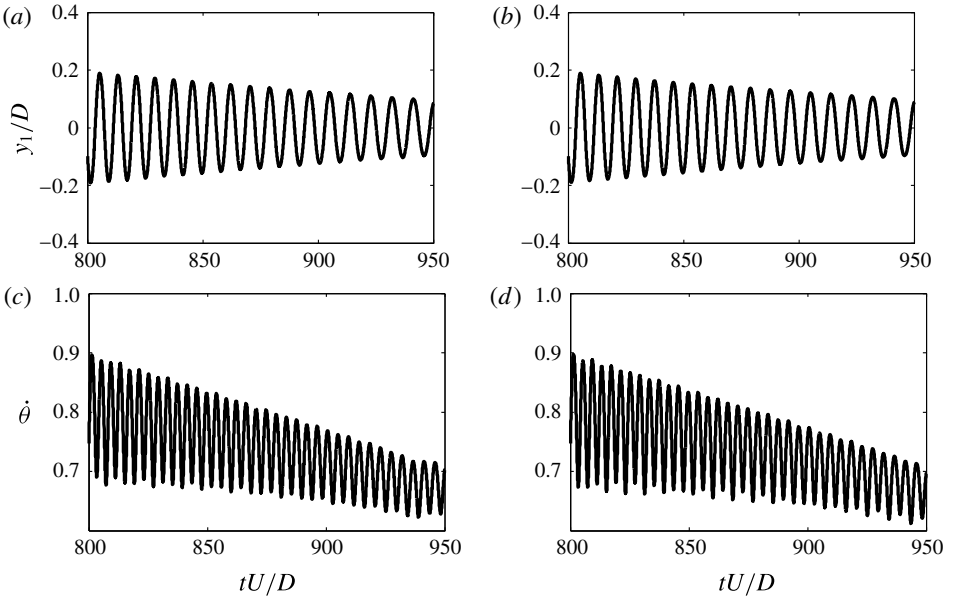

FIGURE 25. For $Re = 100$, $\bar{r}_o = 0.5$, $\epsilon_p = 0.3$ and $\zeta_r = 0.340$, solution of full, PDE-based equations compared to solution of unforced ODE system (with linear damping $\beta = 0.0059$) using initial conditions from PDE solution. (*a*) Cylinder displacement from PDE; (*b*) cylinder displacement from ODE; (*c*) NES angular velocity from PDE; (*d*) NES angular velocity from ODE.

While the cylinder oscillation amplitude falls approximately linearly during slow decay, as seen in figure 23(*a*), the angular velocity of the NES mass falls superlinearly, as seen in figure 23(*c*). Hence, the rate at which rotational kinetic energy of the NES is dissipated falls below the rate at which energy is transferred to the cylinder, and thus the energy of the cylinder must increase. This leads to the bursting associated with the chaotic transition, and after a transient, the relaxation cycle repeats itself. Moreover, our numerical results suggest, but do not prove, that once initiated, the relaxation cycle is robust.

Guided by the above discussion, we model the effect of the flow by introducing an *ad hoc* linear damping term into (6.3*a*), leading to the modified system

$$\frac{\mathrm{d}^2 Y_1}{\mathrm{d}\tau^2} + \beta \frac{\mathrm{d}Y_1}{\mathrm{d}\tau} + \omega_r^{*2} Y_1 = \epsilon_p \bar{r}_o \frac{\mathrm{d}}{\mathrm{d}\tau}\left(\frac{\mathrm{d}\theta}{\mathrm{d}\tau}\sin\theta\right), \tag{6.6a}$$

$$\frac{\mathrm{d}^2\theta}{\mathrm{d}\tau^2} + \frac{\zeta_r}{Re}\frac{\mathrm{d}\theta}{\mathrm{d}\tau} = \frac{\mathrm{d}^2 Y_1}{\mathrm{d}\tau^2}\frac{\sin\theta}{\bar{r}_o}, \tag{6.6b}$$

where the term $\beta \mathrm{d}Y_1/\mathrm{d}\tau$ is used to approximately model the effect of the flow on transverse oscillation of the cylinder during the relaxation cycle. We seek to 'optimize' the approximate model (6.6*a*) and (6.6*b*) by using the PDE solution to prescribe initial conditions for (6.6*a*) and (6.6*b*), and finding the value of β that minimizes the root-mean-square difference between the solution of (6.6*a*) and (6.6*b*) and the PDE response during a slowly decaying portion of the time series. Starting the integration of (6.6*a*) and (6.6*b*) at $tU/D = 800$, with initial conditions $Y_1(800) = -0.098147$, $\mathrm{d}Y_1(800)/\mathrm{d}\tau = -0.13978$, $\theta(800) = 303.57$ and $\mathrm{d}\theta(800)/\mathrm{d}\tau = 0.74668$ from the PDE

solution, we obtain very good agreement of the response with the PDE solution for $\beta = 0.0059$, as seen in figure 25(*a*,*b*) for cylinder displacement, and in figure 25(*c*,*d*) for the NES angular velocity, respectively. The angular displacement of the NES at the end of ODE integration is $\theta(950) = 414.25$ (radians), in excellent agreement with 414.22 predicted from the PDE solution. At this damping value, we can very accurately match the system response if the solution of (6.6*a*) and (6.6*b*) is started at an appropriate time in the slow modulation cycle.

6.3. *Experimental realization*

There are no experimental reports of two-dimensional temporally chaotic flow past a cylinder in this range of Re, except when cylinder vibration is driven externally (Olinger & Sreenivasan (1988); Nakano & Rockwell (1994)), and the only reports of such a flow in a computation also involve external excitation (Li *et al.* (1992); Anagnostopoulos (2000*a*,*b*)). Our prediction of temporally chaotic flow for two-dimensional flow past a sprung circular cylinder with a rotational NES thus raises the question of how the predicted results might be realized experimentally, especially in light of the fact that it is not possible to concentrate all of the mass along a line parallel to the axis of rotation.

As pointed out in § 2.1, the governing equations (2.2*a*,*b*), (2.4*a*,*b*) were derived for the case in which the rotating mass is a 'line mass' concentrated on a line parallel to, and rotating a fixed distance from, the cylinder axis. In part F of the supplementary material, we show that the line mass model is dynamically equivalent to a distributed mass model with a different ratio of the rotating mass to the total mass, and that (according to equations (S20a), (S20b)) the two ratios are related by $\epsilon_p = \epsilon_d \left(R_{cm}/R_g\right)^2$, where R_g and R_{cm} are the radius of gyration and distance from the centre of mass to the axis of rotation, respectively. By 'dynamically equivalent', we mean a situation in which the coefficient of the right-hand side of (2.4*b*) and coefficient of the second term of the right-hand side of (2.4*a*) are identical to the corresponding coefficients in (S19a), (S19b) for the distributed mass case, so that the dynamical response of the distributed mass system is equivalent when m^*, Re, f_n^* and the dissipation parameter ζ_r are the same.

For $\epsilon_p = 0.3$ and $\bar{r}_o = 0.47$ (with $m^* = 10$, $Re = 100$ and $f_n^* = 0.167$), corresponding to the elongated wake solution shown in figure 16, experimental realization is possible using a cylinder with diameter $D = 10$ cm and a free-stream speed of $U = 35$ cm s^{-1} in a 350 cSt lubricating oil with density $\rho_f = 0.89$ g cm^{-3} (e.g. SAE 30 at 20 °C), corresponding to a cylinder density of $\rho_b = 8.9$ g cm^{-3}. As discussed in the supplementary material, dynamic equivalence can be achieved using a rotating tungsten mass (density 19.3 g cm^{-3}) in the shape of a cylinder whose cross-section is that of an annular sector with inner and outer radii of 1 cm and 4.2778 cm, respectively, and sector angle 2.8754 radians, and a stator made of either of two commercially available tungsten alloys with density 17.0 g cm^{-3}, whose inner and outer radii are 4.5766 cm and 5 cm, respectively. (Note that these radii and the sector angle are rounded values of more precisely computed values that correspond to densities of 19.3000 and 17.0000 g cm^{-3} for the rotating mass and stator, respectively. For slightly different densities, the radii and sector angle giving dynamically equivalent response will differ slightly.) This corresponds to a clearance between the rotating mass and stator of slightly more than 2.9 mm. The mass ratio for this arrangement is $\epsilon_d = \hat{M}_{rnes}/(\hat{M}_{stat} + \hat{M}_{rnes}) = 0.6867$, compared to the value of $\epsilon_p = 0.3$ for the dynamically equivalent point/line mass. If the rotating mass lies

beyond the spanwise extent of the flow (e.g. is attached to an unsubmerged shaft extending above a submerged vertical cylinder), then there are no radial constraints on the mass distribution, which greatly simplifies selection of the inertial properties of the rotating mass, and allows dynamic equivalence to be accomplished with a wide range of materials much less dense than tungsten.

7. Conclusions

For a linearly sprung circular cylinder in cross-flow at $Re = 100$, we have shown that vortex-induced vibration can be passively suppressed by targeted energy transfer to a rotating nonlinear energy sink inertially coupled to the rectilinear motion of the cylinder. The similarities between vortex shedding (which gives rise to the fluctuating lift force that drives VIV) for two-dimensional laminar flow past a cylinder at $Re = 100$ and turbulent flow at much higher Re, suggest that this approach might also be feasible well into the turbulent regime. That this approach to VIV suppression is completely passive (requiring no control system, electronics, blowing/suction or power supply), and can be implemented with no geometric modification of the cylindrical surface (by placing the NES inside the cylinder, or attaching it to one or both ends of the cylinder beyond the spanwise extent of the flow domain), increase its attractiveness for applications.

While the NES is indeed a dissipative element, its effects on the flow and cylinder motion (as described in §§ 3–5) are quite different from, and presumably more complex than, what would be expected if proportional damping were to be incorporated directly into the dynamics of the cylinder vibration, i.e. by replacing the second term on the right-hand side of (2.4*a*) by $\gamma \mathrm{d}Y/\mathrm{d}\tau$ (along the lines of Cossu & Morino (2000) and Tumkur *et al.* (2013)). Our results clearly demonstrate the extent to which a rotating NES can alter and enrich the dynamics of VIV. As shown in § 3, the rotating NES not only can suppress the VIV of an NES-less sprung cylinder, but can also destabilize the steady, symmetric, motionless-cylinder solution and excite VIV. The latter is not possible for a system in which dissipation is provided by proportional damping.

Unlike the case of a rectilinear NES (Tumkur *et al.* 2013), in which VIV suppression is effected by TET to a mass whose rectilinear motion is nonlinearly coupled to the parallel or anti-parallel cylinder motion by a nonlinear spring, the rotational NES sometimes gives rise to temporal chaos in the cylinder motion and the flow, as well as to considerable elongation of the region of vorticity attached to the cylinder. We find that temporal chaos and elongation of the attached vorticity are associated with an attractor in which the time series of cylinder displacement resembles a relaxation oscillation cycle, consisting of slowly decaying oscillations separated by rapid chaotic bursting. The elongation of the vortex, and its relationship to the (unstable) steady symmetric flow past a fixed cylinder at $Re = 100$, suggest that continuous transfer of energy from the flow to the cylinder, and subsequent dissipation by the NES, can partially stabilize the steady symmetric flow during the slow decay.

The elongated wake solution was found to have an increased NES-induced effective mass, leading to a shift in the response frequency away from the Strouhal frequency. The slow decay in response, and the frequency shift approximated by our analytical model, both match those of the solution of the full problem. The slowly decaying oscillation of the cylinder displacement can also be approximated by a simple model of the cylinder and rotational NES, in which the only interaction with the flow is

through an empirical linear damping term. The elongated wake solution and associated slow decay in cylinder displacement are found to exist over a range of *Re* and NES parameters.

Our results show that the addition of a purely passive, strongly nonlinear, rotating dissipative attachment to a bluff body undergoing VIV, can not only suppress VIV of the body, but also drastically change the topology of the wake, and, hence, the corresponding drag and lift coefficients of the body. Moreover, such an attachment can induce chaos at intermediate *Re*.

Acknowledgements

The authors thank Professors D. J. Olinger and K. R. Sreenivasan for helping us understand their experimental results. We also thank Professor P. F. Fischer for help in using Nek5000. The authors also thank an anonymous reviewer, whose persistence led to the discussion of dissipation and damping in the penultimate paragraph of § 2.1. The authors gratefully acknowledge partial support from NSF grant CMMI-1363231. They also acknowledge use of the Taub cluster parallel computing resource provided by the Computational Science and Engineering Program at the University of Illinois, and the facilities of the Extreme Science and Engineering Discovery Environment (XSEDE), supported by National Science Foundation grant OCI-1053575.

Supplementary materials

Supplementary materials are available at https://doi.org/10.1017/jfm.2017.504.

REFERENCES

ANAGNOSTOPOULOS, P. 2000*a* Numerical study of the flow past a cylinder excited transversely to the incident stream. Part 1. Lock-in zone, hydrodynamic forces and wake geometry. *J. Fluids Struct.* **14**, 819–851.

ANAGNOSTOPOULOS, P. 2000*b* Numerical study of the flow past a cylinder excited transversely to the incident stream. Part 2. Timing of vortex shedding, aperiodic phenomena and wake parameters. *J. Fluids Struct.* **14**, 853–882.

ANAGNOSTOPOULOS, P. & BEARMAN, P. W. 1992 Response characteristics of a vortex-excited cylinder at low Reynolds numbers. *J. Fluids Struct.* **6**, 39–50.

ARGOUL, P. & LE, T.-P. 2003 Instantaneous indicators of structural behaviour based on the continuous cauchy wavelet analysis. *Mech. Sys. Sign. Proc.* **17**, 243–250.

ARNOL'D, V. I. 1988 *Dynamical Systems III, Encyclopaedia of Mathematical Sciences*. Springer.

BAEK, S.-J. & SUNG, H. J. 2000 Quasi-periodicity in the wake of a rotationally oscillating cylinder. *J. Fluid Mech.* **408**, 275–300.

BATCHO, P. & KARNIADAKIS, G. E. 1991 Chaotic transport in two- and three-dimensional flow past a cylinder. *Phys. Fluids* A **3**, 1051–1062.

BEARMAN, P. W. 1984 Vortex shedding from oscillating bluff bodies. *Annu. Rev. Fluid Mech.* **16**, 195–222.

BEARMAN, P. W. 2011 Circular cylinder wakes and vortex-induced vibrations. *J. Fluids Struct.* **27**, 648–658.

BLACKBURN, H. & HENDERSON, R. 1996 Lock-in behavior in simulated vortex-induced vibration. *Exp. Therm. Fluid Sci.* **12**, 184–189.

CALDERER, R. & MASUD, A. 2010 A multiscale stabilized ALE formulation for incompressible flows with moving boundaries. *Comput. Mech.* **46**, 185–197.

CHUNG, J. & HULBERT, G. M. 1993 A time integration algorithm for structural dynamics with improved numerical dissipation: the generalized-α method. *Trans. ASME J. Appl. Mech.* **60**, 371–375.

COSSU, C. & MORINO, L. 2000 On the instability of a spring-mounted circular cylinder in a viscous flow at low Reynolds numbers. *J. Fluids Struct.* **14**, 183–196.

DAUCHY, C., DUŠSEK, J. & FRAUNIÉ, P. 1997 Primary and secondary instabilities in the wake of a cylinder with free ends. *J. Fluid Mech.* **332**, 295–339.

DESHMUKH, S. R. & VLACHOS, D. G. 2005 Novel micromixers driven by flow instabilities: application to post-reactors. *AIChE J.* **51**, 3193–3204.

FISCHER, P. F., LOTTES, J. W. & KERKEMEIER, S. G. 2008 nek5000 Web page. http://nek5000.mcs.anl.gov.

GABBAI, R. D. & BENAROYA, H. 2005 An overview of modeling and experiments of vortex-induced vibration of circular cylinders. *J. Sound Vib.* **282**, 575–616.

GENDELMAN, O. V. 2011 Targeted energy transfer in systems with external and self-excitation. *Proc. Inst. Mech. Engrs* C **225**, 2007–2043.

GENDELMAN, O. V., SIGALOV, G., MANEVITCH, L. I., MANE, M., VAKAKIS, A. F. & BERGMAN, L. A. 2012 Dynamics of an eccentric rotational nonlinear energy sink. *J. Appl. Mech. Trans. ASME* **79**, 011012-9.

GRASSBERGER, P. & PROCACCIA, I. 1983 Characterization of strange attractors. *Phys. Rev. Lett.* **50**, 346–349.

GROSSMANN, A. & MORLET, J. 1984 Decomposition of Hardy functions into square integrable wavelets of constant shape. *SIAM J. Math. Anal.* **15**, 723–736.

HARRIS, F. J. 1978 On the use of windows for harmonic analysis with the discrete Fourier transform. *Proc. IEEE* **66**, 51–83.

HEGGER, R., KANTZ, H. & SCHREIBER, T. 1999 Practical implementation of nonlinear time series methods: the TISEAN package. *Chaos* **9**, 413–435.

HENDERSON, R. D. 1995 Details of the drag curve near the onset of vortex shedding. *Phys. Fluids* **7**, 2102–2104.

JANSEN, K. E., WHITING, C. H. & HULBERT, G. M. 2000 A generalized-α method for integrating the filtered Navier–Stokes equations with a stabilized finite element method. *Comput. Meth. Appl. Mech. Engng* **190**, 305–319.

KARNIADAKIS, G. E. & TRIANTAFYLLOU, G. S. 1989 The crisis of transport measures in chaotic flow past a cylinder. *Phys. Fluids* A **1**, 628–630.

LEE, J. H. & BERNITSAS, M. M. 2011 High-damping, high-Reynolds VIV tests for energy harnessing using the VIVACE converter. *Ocean Engng* **38**, 1697–1712.

LEONTINI, J. S., THOMPSON, M. C. & HOURIGAN, K. 2006 The beginning of branching behaviour of vortex-induced vibration during two-dimensional flow. *J. Fluids Struct.* **22**, 857–864.

LEONTINI, J. S., THOMPSON, M. C. & HOURIGAN, K. 2007 Three-dimensional transition in the wake of a transversely oscillating cylinder. *J. Fluid Mech.* **577**, 79–104.

LI, J., SUN, J. & ROUX, B. 1992 Numerical study of an oscillating cylinder in uniform flow and in the wake of an upstream cylinder. *J. Fluid Mech.* **237**, 457–478.

MITTAL, S. & SINGH, S. 2005 Vortex-induced vibrations at subcritical *Re*. *J. Fluid Mech.* **534**, 185–194.

NAKANO, M. & ROCKWELL, D. 1994 Flow structure in the frequency-modulated wake of a cylinder. *J. Fluid Mech.* **266**, 93–119.

OLINGER, D. J. 1993 A low-dimensional model for chaos in open fluid flows. *Phys. Fluids* A **5**, 1947–1951.

OLINGER, D. J. & SREENIVASAN, K. R. 1988 Nonlinear dynamics of the wake of an oscillating cylinder. *Phys. Rev. Lett.* **60**, 797–800.

PAÏDOUSSIS, M. P., PRICE, S. J. & DE LANGRE, E. 2011 *Fluid-Structure Interactions: Cross-Flow-Induced Instabilities*. Cambridge University Press.

PRASANTH, T. K. & MITTAL, S. 2009 Vortex-induced vibration of two circular cylinders at low Reynolds number. *J. Fluids Struct.* **25**, 731–741.

PULLIAM, T. H. & VASTANO, J. A. 1993 Transition to chaos in an open unforced 2D flow. *J. Comput. Phys.* **105**, 133–149.

ROSHKO, A. 1954 On the drag and shedding frequency of two-dimensional bluff bodies. *National Advisory Committee for Aeronautics, TN* 3169.

SARPKAYA, T. 2004 A critical review of the intrinsic nature of vortex-induced vibrations. *J. Fluids Struct.* **19**, 389–447.

SHIELS, D., LEONARD, A. & ROSHKO, A. 2001 Flow-induced vibration of a circular cylinder at limiting structural parameters. *J. Fluids Struct.* **15**, 3–21.

SREENIVASAN, K. R. 1985 Transition and turbulence in fluid flows and low-dimensional chaos. In *Frontiers in Fluid Mechanics* (ed. S. H. Davis & J. L. Lumley), pp. 41–67. Springer.

TUMKUR, R. K. R., CALDERER, R., MASUD, A., PEARLSTEIN, A. J., BERGMAN, L. A. & VAKAKIS, A. F. 2013 Computational study of vortex-induced vibration of a sprung rigid circular cylinder with a strongly nonlinear internal attachment. *J. Fluids Struct.* **40**, 214–232.

TUMKUR, R. K. R., FISCHER, P. F., BERGMAN, L. A., VAKAKIS, A. F. & PEARLSTEIN, A. J. 2017 Stability of the steady, two-dimensional flow past a linearly-sprung circular cylinder. *J. Fluid Mech.* (submitted).

VAKAKIS, A. F., GENDELMAN, O. V., BERGMAN, L. A., MCFARLAND, D. M., KERSCHEN, G. & LEE, Y. S. 2008 *Nonlinear Targeted Energy Transfer in Mechanical and Structural Systems,* Vol. I and II. Springer.

VAN ATTA, C. W. & GHARIB, M. 1987 Ordered and chaotic vortex streets behind circular cylinders at low Reynolds numbers. *J. Fluid Mech.* **174**, 113–133.

WILLIAMSON, C. H. K. 1988 The existence of two stages in the transition to three-dimensionality of a cylinder wake. *Phys. Fluids* **31**, 3165–3168.

WILLIAMSON, C. H. K. 1989 Oblique and parallel modes of vortex shedding in the wake of a circular cylinder at low Reynolds numbers. *J. Fluid Mech.* **206**, 579–627.

WILLIAMSON, C. H. K. 1996 Vortex dynamics in the cylinder wake. *Annu. Rev. Fluid Mech.* **28**, 477–539.

WILLIAMSON, C. H. K. & GOVARDHAN, R. 2004 Vortex-induced vibrations. *Annu. Rev. Fluid Mech.* **36**, 413–455.

WILLIAMSON, C. H. K. & ROSHKO, A. 1988 Vortex formation in the wake of an oscillating cylinder. *J. Fluids Struct.* **2**, 355–381.

ZIELINSKA, B. J. A. & WESFREID, J. E. 1995 On the spatial structure of global modes in wake flow. *Phys. Fluids* **7**, 1418–1424.